UNIVERSITY OF TARTU
Faculty of Science and Technology
Institute of Technology

Amina Alimbekova

# Mechanochemical Production of Non-Precious Bifunctional Fe-N-C Electrocatalysts

Bachelor's Thesis (12 ECTS)

Curriculum Science and Technology

Supervisors:
Akmal Kosimov, M.Sc
Nadežda Kongi, Ph.D

Tartu 2022

# Mechanochemical Production of Non-Precious Bifunctional Fe-N-C Electrocatalysts

**Abstract:**

Bifunctional catalyst materials development for energy storage and conversion technologies presents a set of issues in terms of electrochemistry and synthesis. These issues include low stability, sluggish kinetics, and high total overpotential (ΔE), as well as environmental safety, production methodologies, and cost. Noble metal electrocatalysts are used as benchmark catalysts due to their satisfactory bifunctional activity. However, ecological and economic sustainability is severely compromised due to the scarcity of these metals. As an alternative, first-row transition metal heteroatom-doped carbon materials can be utilized. Such noble metal-free catalysts can provide great activity and stability for both oxygen reduction reaction (ORR) and oxygen evolution reaction (OER) while maintaining low costs and high availability of precursors. This work demonstrates a high-performance Fe-N-C type material with sustainable synthesis and favorable activity regarding the ORR and OER. The proposed methodology uses sacrificial templates combined with mechanochemistry, which results in materials with efficient bifunctional catalysts performance that matches the benchmark Pt/Ru-based catalysts.

**Keywords:**

bifunctional catalysts, mechanochemistry, metal-nitrogen-carbon, metal-air battery

**CERCS:** P401 Electrochemistry, T140 Energy Research, T150 Material Technology

## Väärismetallivabade Bifunktsionaalsete Fe-N-C Elektrokatalüsaatorite Mehhanokeemiline Tootmine

**Lühikokkuvõte:**

Bifunktsionaalsete katalüsaatormaterjalide arendamisel energia salvestamise ja muundamise tehnoloogiate jaoks esineb mitu elektrokeemiaga ja sünteesiga seotud väljakutseid. Nende probleemide hulka kuuluvad materjalide madal stabiilsus, aeglane kineetika ja suur summaarne ülepinge (ΔE), samuti keskkonnaohutus, keerulised tootmismeetodid ja kõrge hind. Hetkel kasutatakse väärismetallidel põhinevaid elektrokatalüsaatoreid nende kõrge elektroaktiivsuse tõttu. Ökoloogiline ja majanduslik jätkusuutlikkus on aga nende väärismetallide nappuse tõttu tõsiselt ohus. Alternatiivina võib kasutada siirdemetallide ja heteroaatomitega dopeeritud süsinikmaterjale. Sellised väärismetallivabad katalüsaatorid võivad olla väga aktiivsed ja stabiilsed nii hapniku redutseerimisreaktsiooni (ORR) kui ka hapniku eraldumise reaktsiooni (OER) jaoks, säilitades samal ajal madalad tootmiskulud ja lähteainete kõrge kättesaadavuse. Antud bakalaureusetöös on välja töötatud jätkusuutlik metoodika kõrge elektroaktiivsusega Fe-N-C tüüpi materjali sünteesiks. Antud metoodikas rakendatakse uudsed mehhanokeemilised sünteesivõtted, mille tulemusena valmib kõrge elektroaktiivsusega bifunktsionaalne katalüsaatormaterjal.

**Võtmesõnad:**

bifunktsionaalsed katalüsaatorid, mehhaanokeemia, metall-lämmastik-süsinik, metall-õhk aku

**CERCS:** P401 Elektrokeemia, T140 Energeetika, T150 Materjalitehnoloogia

# TABLE OF CONTENTS

TERMS, ABBREVIATIONS, AND NOTATIONS ..... 5

INTRODUCTION ..... 6

1 LITERATURE REVIEW ..... 7

1.1 Energy Storage and Conversion as a Solution ..... 7

1.2 Metal-Air Batteries. An Overview ..... 8

1.3 Introduction to Bifunctional Oxygen Electrocatalysis ..... 9

1.3.1 Electrochemical Characterization Basics of Oxygen Reduction Reaction and Oxygen Evolution Reaction ..... 9

1.3.2 Materials Involved in Bifunctional Oxygen Electrocatalysis ..... 11

2 THE AIMS OF THE THESIS ..... 16

3 EXPERIMENTAL PART ..... 17

3.1 MATERIALS AND METHODS ..... 17

3.1.1 Chemicals and Materials ..... 17

3.1.2 Catalyst Synthesis ..... 17

3.1.3 Physical characterization ..... 18

3.1.4 Electrochemical characterization ..... 20

3.2 RESULTS AND DISCUSSION ..... 23

3.2.1 Synthesis ..... 23

3.2.2 Physical characterization ..... 24

3.2.3 Electrochemical characterization ..... 29

3.2.4 Zn-Air Battery Performances ..... 37

SUMMARY ..... 40

ACKNOWLEDGEMENTS ..... 41

REFERENCES ..... 42

Non-exclusive licence to reproduce the thesis and make the thesis public ..... 47

## TERMS, ABBREVIATIONS, AND NOTATIONS

| | |
|---|---|
| APS | average pore size |
| BET | Brunauer-Emmet-Teller |
| CV | cyclic voltammetry |
| (E)ESC | (electrochemical) energy storage and conversion |
| (E)DLC | (electrochemical) double layer capacitance |
| $E_{1/2}$ | half-wave potential |
| ECSA | electrochemical surface area |
| $E_{j=10}$ | potential at a current density equal to 10 mA $cm^{-2}$ |
| $E_{onset}$ | onset potential |
| GC | glassy carbon |
| IPA | isopropyl alcohol |
| K-L | Koutecky–Levich |
| LAC | liquid-assisted compression |
| LAG | liquid-assisted griding |
| LIB | li-ion battery |
| MAB | metal-air battery |
| M-N-C | metal-nitrogen-carbon |
| MP-AES | microwave plasma atomic emission spectroscopy |
| OER | oxygen evolution reaction |
| ORR | oxygen reduction reaction |
| PGM | platinum group metals |
| PXRD | powder x-ray diffraction |
| QSDFT | quenched solid density functional theory |
| RDE | rotating disc electrode |
| RHE | reversible hydrogen electrode |
| SAC | single-atom catalyst |
| SEM | scanning electron microscopy |
| XPS | x-ray photoelectron spectroscopy |
| ZAB | zinc-air battery |
| η | overpotential |

# INTRODUCTION

The energy crisis of recent years accelerated the plans for the transition toward renewable energy alternatives. These technologies are typically held to a higher standard since they must be secure, sustainable, cost-effective, and efficient [1]. However, renewable energy lacks security as its supply is not always continuous and may not fulfill the demands [2]. Therefore, there is a need for an agile technology to convert and store the incoming energy smartly. In this regard, metal-air batteries (MABs) serve as energy storage and conversion (ESC) technologies. The principal mechanisms of this device are oxygen reduction and evolution reactions (ORR and OER, respectively) on the catalyst-supported cathode, along with a redox reaction of metal on the anode. The intelligently designed catalyst material is a fundamental aspect of the rechargeable MAB to sustain efficient ORR and OER. Current benchmark catalysts contain carbon-supported platinum group metals and metal oxides (e.g., Pt, Ir, Ru, etc.). However, sufficient activity is offset by high costs and scarcity of materials. An alternative approach is to use heteroatom doped (e.g., N) carbon materials decorated with earth-abundant metals (e.g., Fe, Ni, Co, etc.) to enhance the ORR/OER activity and catalyst stability.

Common synthesis strategies include carbonization of nitrogen-rich organic precursors with a metallic salt, doping carbon nanomaterials with metals and nitrogen, or template-assisted aggregation of carbon-based materials. Most of the popular methods heavily rely on wet chemistry methods, which may result in a large volume of unrecyclable waste solvent. One of the potential alternatives is mechanochemical production of the bifunctional catalysts via induction of chemical change through mechanical impact. Benefits of such material preparation include straightforward protocols, resource-efficient processes, reduction of chemical waste, more effortless scalability, and higher material output [3].

In this work, Fe-N-C type bifunctional ORR/OER electrocatalysts were prepared through the mechanochemical ball milling and compression steps. A set of physical characterization methods were used to analyze catalysts' structure, morphology, and porosity (namely SEM, XPS, MP-AES, XRD, and $N_2$ physisorption). The electrochemical performance of prepared electrocatalysts was studied in a conventional three-electrode setup, and catalyst' practical performance in Zn-air battery was investigated.

# 1 LITERATURE REVIEW

## 1.1 Energy Storage and Conversion as a Solution

Ever-growing energy demand and traditional ways of energy consumption via fossil fuels result in socioeconomic, geopolitical, and ecological issues that will be a pressing matter in the present and the future. Some of the global energy problems manifest in energy access and renewability. This awareness leads to a necessity to transition to clean and sustainable energy technologies [4], [5].

Renewable solar and wind power provide a continuous yet sporadic energy source, so it is necessary to develop storage systems to efficiently reserve and utilize the energy. This is especially crucial to meaningfully integrate renewable energy sources into the grid. This can be achieved through rapid and efficient response to energy demand. Specifically, the flexibility of renewable energy sources should manifest itself in optimizing the use of electricity during on/off-peak [6], [7].

In recent years, the emergence of electrochemical energy storage and conversion (ESC) devices, such as batteries, fuel cells, and supercapacitors, facilitated the move towards more viable energy. The working principle of this technology is the utilization of chemical compounds and redox reactions to convert and store the electrical power. Such devices can potentially reduce the supply-demand discrepancy while providing reliable, inexpensive, portative, and clean energy sources [8].

The electrical energy can be generated via redox reactions in the electrochemical cell, as with batteries and fuel cells. A battery is a closed system of connected cells composed of positive and negative electrodes where the charge transfer reaction happens. While having a similar working principle, fuel cells are open systems where the reactants, or the fuel, for the redox reaction are delivered into the cell externally [7], [9].

In terms of the energy and power density of these systems, fuel cells are high-energy and low-power devices, while batteries typically show average energy and power characteristics [9]. However, it is essential to note that these characteristics can often overlap. In general, particular hybrid systems usually have intermediate values [10].

Currently, one of the most popular alternatives for EESC is Li-ion batteries (LIBs). They are widely utilized in various portable devices and electric vehicles due to their sufficient specific energy and high specific power values. However, improvements to these batteries are

required to complete the supply-demand and the storage of energy at a large scale. Finally, high cost, an insufficient supply of raw materials, complex recycling practices, and safety risks further make the Li-ion batteries a less favorable option for the future [9]–[11].

## 1.2 Metal-Air Batteries. An Overview

Metal-air batteries (MABs), which are usually viewed as a cross between a battery and a fuel cell, operate on externally supplied oxygen (reagent). As a result, the total weight of the cell is reduced, leading to higher energy density values than conventional LIBs. This resulted in MABs becoming a desirable option for ESC devices. In addition, the abundance of materials for MABs makes them a low-cost, reliable, safe, and environmentally friendly solution without significant compromises in their efficiency and energy density [9]–[11].

The MAB commonly consists of four parts: a metal anode, a cathode in the form of an air electrode, a suitable separator, and an electrolyte solution. Typically, the air-breathing electrode is a porous cathode that absorbs atmospheric oxygen, while the metal electrode is an anode constructed from alkali (e.g., Li), earth-abundant (e.g., Al), and transition (e.g., Fe, Ni, Co) metals [12], [11], [13]. The anode is also saturated with the suitable electrolyte solution, and the two electrodes are separated with a separator. This structural difference allows for a less bulky system while reaching a high theoretical energy density in the range of 1353–11429 Wh $kg^{-1}$ (calculated by the common Zn-, Al-, Mg- and Li-air batteries), which are about 3–30 times higher than that of lithium-ion battery [13].

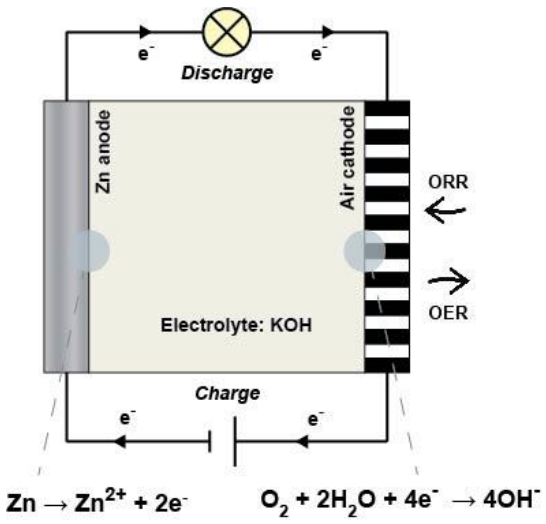


Figure 1. Schematic representation of a Zn-air battery.

The working principle of a MAB in an alkaline media can be described by discharging and charging reactions as follows (Fig. 1). For the discharging process, oxidation takes place on the metallic anode. Once the electrons are released, metal ions combine with the hydroxide ions from the electrolyte to form a metal hydroxide:

$$M + nOH^- \rightarrow M(OH)_n + ne^- \quad (1)$$

Reduction, on the other hand, takes place on the air cathode. The released electrons from oxidation reach the cathode to participate in the reaction:

$$\frac{n}{4}O_2 + ne^- + \frac{n}{2}H_2O \rightarrow nOH^- \quad (2)$$

Here, oxygen molecules combine with electrons and water to form hydroxide ions. These ions complete the circuit by being transported through the separator.

Thus, the overall reaction is:

$$M + \frac{n}{4}O_2 + \frac{n}{2}H_2O \rightarrow M(OH)_n \quad (3)$$

## 1.3 Introduction to Bifunctional Oxygen Electrocatalysis

### 1.3.1 Electrochemical Characterization Basics of Oxygen Reduction Reaction and Oxygen Evolution Reaction

The electrical power in such cases is discharged through the oxidation of metallic anode and reduction of atmospheric oxygen via oxygen reduction reaction. The charging of MAB is possible by storing the electrical energy generated through the oxygen evolution reaction [11]. Specific intrinsic properties of the reactions cause sluggish kinetics and therefore require the usage of electrocatalysts. Designing efficient MABs typically requires that the material can be used to catalyze both the ORR and OER (i.e., be bifunctional). While numerous catalysts have been developed separately for ORR [14] and OER [15], it is challenging to create a bifunctional catalyst that would be stable across both ORR and OER potentials [16]. The primary reason for such requirements arises from the molecular bases of the ORR and OER, which are described as follows.

Two pathways are possible for ORR in aqueous solutions [17]:

- Direct – four-electron reduction: $O_2$ to $H_2O$

$$O_2 + 2H_2O + 4e^- \rightarrow 4OH^- \quad (4)$$

- Indirect – two-electron reduction: $O_2$ to $H_2O_2$ [17]

$$O_2 + H_2O + 2e^- \rightarrow HO_2^- \quad (5)$$

$$HO_2^- + H_2O + 2e^- \rightarrow 3HO^- \quad (6)$$

$$2HO_2^- \rightarrow 2HO^- + O_2 \quad (7)$$

Since this work mainly focuses on metal-air batteries, the reduction to water is preferred. The four-electron reduction can take place via two processes:

- Dissociative mechanism
- Associative mechanism

In the first case, $O_2$ adsorbs to the catalyst surface and splits to form atomic oxygen. Next, it undergoes a reduction by two electrons to form $H_2O$. This can be described by equations [18]:

$$O_2 + free\ active\ site \rightarrow 2O(adsorbed) \quad (8)$$

$$O(adsorbed) + H^+ + e^- \rightarrow HO(adsorbed) \quad (9)$$

$$HO(adsorbed) + H^+ + e^- \rightarrow H_2O + free\ active\ site \quad (10)$$

ORR via dissociative pathway does not stabilize $O_2$ on the catalyst surface, so $H_2O_2$ cannot be produced. On the other hand, in the associative mechanism, the $O_2$ is not immediately split on the catalyst surface:

$$O_2 + free\ active\ site \rightarrow O_2(adsorbed) \quad (11)$$

$$O_2(adsorbed) + H^+ + e^- \rightarrow HOO(adsorbed) \quad (12)$$

$$HOO(adsorbed) + free\ active\ site \rightarrow HO(adsorbed) + O(adsorbed) \quad (13)$$

It can be seen from these reactions that the kinetics are limited by the transfer of the first electron from the cathode to oxygen, the hydration of the oxygen, and the desorption of the intermediate structures [18].

OER can occur as a reverse reaction of either of the two pathways. For example, OER reaction via associative mechanism:

$$H_2O + free\ active\ site \rightarrow HO(adsorbed) + H^+ + e^- \quad (14)$$

$$HO(adsorbed) \rightarrow O(adsorbed) + H^+ + e^- \quad (15)$$

$$H_2O + O(adsorbed) \rightarrow HOO(adsorbed) + H^+ + e^- \quad (16)$$

$$HOO(adsorbed) \rightarrow free\ active\ site + O_2 + H^+ + e^- \quad (17)$$

Essentially OER is electrochemical water splitting reaction [19]:

$$2H_2O = 2H_2 + O_2 \quad (18)$$

It is important to note, that these reactions are crude simplifications of the actual processes. Nevertheless, they are still helpful for understanding the conditions for ORR and OER and challenges for catalysis. First, it is evident that the free energy of adsorption of the intermediate should be such so that the reactions take place close to equilibrium potential. However, no such catalyst has been discovered yet, and the overpotential is considered to be intrinsic to these processes [20]. In addition, if a catalyst material is perfect for ORR, it might not be suitable for OER. One of the reasons for this might be that OER functions at higher anodic potentials, leading to oxidation of certain materials. When considering bifunctional ORR/OER catalysis, the limiting steps for the activity of each of the process is different: $O_2$ reduction and HO(ads) for ORR and O(ads) and HOO(ads) formation for OER. Besides, the binding energies of the intermediates (e.g., O(ads), HO(ads), and HOO(ads)) are different for ORR and OER, which means that efficient catalysis for one of them may not be perfectly suitable for the other [21].

### 1.3.2 Materials Involved in Bifunctional Oxygen Electrocatalysis

Since the binding strength of the intermediate structures for OER and ORR is different, the bifunctional material should be suitable to operate at reversible conditions necessary for MABs [16]. Over the years, numerous bifunctional oxygen catalysts have been developed, including noble metals [22], [23], noble-metal-based alloys or composites [23], [24], noble-metal-free transition metal oxides (TMO) [25], [26], perovskites [27], [28], carbon materials [29], [30], metal or metal-oxide/ carbon composites [25], as well as the single-atom catalysts [31].

Currently, the benchmark bifunctional catalyst materials are platinum group metals (PGM), namely Ru, Ir, and Pt [18]. However, certain disadvantages are associated with the most efficient catalysts. Platinum (Pt), for example, is a suitable catalyst for ORR but unsuitable

for OER due to the generation of an oxide layer that is less conductive electrically. Another metal, ruthenium (Ru), shows superior OER activity while being inferior in terms of ORR. Notably, the Ru catalyst might experience corrosion at the potentials associated with ORR, so oxide – $RuO_2$ – is typically used in these cases. Similarly, iridium (Ir) shows a good bifunctionality, but experiences oxidation during OER, so in the following cycles, it shows suppressed activity towards ORR [8]. To achieve the desired bifunctionality, a common strategy is to combine the metals into a composite catalyst, such as PtRu material, so that Pt and Ru function as catalysts for ORR and OER, respectively [16]. It is important to note that discussions about PGM catalysts rarely involve pure metals. As such, these catalysts are usually metal or metal oxide nanoparticles incorporated with amorphous carbon as a support. While PGM catalyst materials are considered the state-of-the-art benchmark catalysts, their bifunctionality may still not be sufficient in terms of durability and stability. Besides, the scarcity and high cost of these catalysts limit their use as a sustainable ESC solution.

In order to solve the cost and scarcity problems, carbon PGM-free materials have been developed to fit the activity parameters comparable to the benchmark catalysts [32]. Carbon precursors for the catalyst materials are also easily tunable, so the catalyst activity can be enhanced by incorporating various compounds. One of the possibilities to alter the carbon structures is the introduction of non-metal atoms. Doping of carbon-based catalyst material is a technique in which some carbon atoms are substituted with other atoms, such as N, B, S, and P. In these cases, the electron configuration of adjacent carbons is altered, which leads to changing of the carbon sp2 plane electroneutrality due to size and electronegativity differences. These factors, in turn, provide the adsorption sites for catalysis [16]. For example, N-doping promotes the formation of graphitic, pyridinic, and pyrrolic nitrogen sites. In pyridinic N, the structure is reminiscent of the benzene hybridized sp2 plane. The electronegativity of N results in a higher number of attractive sites for electron adsorption, making reactions more likely to proceed. The N-content has also been observed in direct correlation to ORR activity [33]. In addition, nitrogen is more likely to enter the carbon structure due to its similar sizes. N doping is usually achieved using a carbon precursor containing nitrogen or annealing carbon in a nitrogen atmosphere [34]. Overall, the increasing desire for more sustainable and “green” ESC devices makes carbon based materials a promising choice for the development of high-performance bifunctional heteroatom-doped catalysts for ORR/OER.

Electrocatalytic activity can be further enhanced by introducing metals to heteroatom doped carbon matrix to produce M-N-C type material, where M stands for the selected metal. First-row transition metals, like Fe, Ni, and Co, can be introduced to improve the bifunctional activity. Among possible structures, single-atom catalysts (SACs) are typically viewed as one of the prominent research topics [14], [21], [35]. In SACs, the active centers of electrocatalysis are Fe-$N_x$ (x = 4, 5, 6), which represent the N-coordinated Fe configurations. Single-atom dispersion is favored mainly due to the smaller size of the introduced metallic centers, which changes the atomic and electronic structure of the catalyst matrix. This, in turn, causes the molecular surface to become heterogeneous. As a result, the number of exposed active sites that favor the ORR and OER reactions increases. [21]

The research of M-N-C type electrocatalysts has started with the work by Jasinski (1964) [36] on ORR catalysts based on cobalt phthalocyanine using transition metal macrocycles. Later, Gupta et al. (1989) [37] developed an alternative practice where transition metal macrocycles are replaced by separate nitrogen and metal precursors to create an active catalyst. These articles provided the framework for future work on catalyst design, with recent research exploring various synthetic strategies for Fe-N-C catalysts. As such, state of the art material synthesis approaches range from "traditional" pyrolysis of metal salts and N-, C-containing precursors to wood-based SACs.

For instance, Lyu et al. (2018) [38] reported the bifunctional catalyst with the activity parameters: ORR $E_{1/2}$ = 0.91 V, OER $E_{j=10}$ = 1.61 V and $\Delta E$ = 0.70 V in 0.1M KOH. The Fe-N-C material was synthesized through pyrolyzing poly{2,6-bis-[2-(N-(8-amino-naphthalen-1-yl)-imino)ethyl] pyrydine} iron trichloride complex. The catalyst was created using 2,6-Diacetylpyridine (DAP) and 1,8-Diamino-naphthalene (DAN) as precursors with $FeCl_3 \cdot 6H_2O$ as the iron source. The morphology studies revealed spherical structures with a relatively high surface area (up to 1796 $m^2\ g^{-1}$). The molecular structure is represented by N-doped highly graphitized carbon with single-atom iron in Fe-$N_5$ configurations. The catalyst was synthesized without using any support templates. The authors suggest that uniform dispersion of Fe-$N_5$ sites in highly graphitized carbon in a catalytic material is possible through a sensible selection of precursors.

Porous structures for efficient bifunctional activity can also be produced by forming a single-atom catalyst by decorating carbon walls from a wood precursor with iron atoms using a Lewis acid, as described by Zhong et al. [39]. This synthesis technique results in a micro- and mesoporous catalyst with the recorded half-wave and onset potentials equaling 0.85 V

and 0.99 V, respectively. The bifunctional activity for the best performing sample was $\Delta E = E_{j=10} - E_{1/2} = 0.79$ V.

Several works describe the deposition of catalysts on the water-soluble crystalline structures that are etched away later to create hollows in the material. For example, Zhang et al. [40] assessed the activity of the Fe-N-C material in 0.1 M KOH, with the results being $E_{1/2}$ = 0.872 V, $E_{onset}$ = 1.02 V, $E_{j=10}$ = 1.753 V. The bifunctional activity of the material was evaluated as $\Delta E$ = 0.881 V. The synthesis of Fe-N-C was based on 2-aminoterephthalic acid as a carbon base, N-dimethylformamide as a nitrogen precursor, and FeCl3 as an iron source. The hollow structures were achieved by dispersing the precursors with tannic acid crystals, followed by the etching process. The Fe-N-C material has a fluffy and wrinkled nanosheet structure.

Guo et al. [41] described a similar idea, where iron chloride ($FeCl_3 \cdot 6H_2O$) and triazine (2,4,6-tri(2-pyridyl)-1,3,5-triazine) are dissolved with potassium oxalate ($K_2C_2O_4 \cdot H_2O$) as a pore-activator and sodium chloride (NaCl) to achieve a sheet-like catalyst. However, the reported activity does not include the OER activity and only discusses ORR performance, with half-wave and onset potentials equaling 0.86 V and 1.02 V, respectively.

The mentioned articles show that solvent-based synthesis strategies are typically employed for Fe-N-C material development. Mechanochemistry, which refers to the practice of using kinetic force to induce a chemical reaction, can be utilized to make the production process more sustainable. Unlike wet chemistry methods, mechanochemistry requires little to no solvents. Even if some liquid is used, as in the case with liquid-assisted grinding, its amounts are negligible to account for the solubility of the mixture in catalyst structure formation [42]. In this case, centrifugal force or high pressures are applied to the precursors loaded into the ball mill or a compression chamber. Advantages of this method include its straightforwardness, solvent waste minimization, and improved scalability. As a result, this approach becomes one of the most viable options for catalyst production in an industrial setting [3], [43].

Recently, Kosimov et al. [44] proposed a mechanochemical approach for the cobalt-based catalyst preparation with 2,4,6-tri(2-pyridyl)-1,3,5-triazine and a metal salt as precursors and NaCl as a template for synthesizing an active M-N-C type catalyst. The suggested solid-phase production involves grinding and compressing the precursors using minimal amounts of mild solvents (ethanol in this case). This process lends itself to a large-scale synthesis protocol of an accessible and sustainable catalyst. The described oxygen reduction reaction

activities of the best performing Co-N-C catalyst are $E_{1/2}$ = 0.83 V and $E_{onset}$ = 0.98 V. The product of liquid assisted grinding and compression method (i.e., the material was ground and then compressed) displayed high porosity, an abundance of pyridinic-N sites, as well as small and dispersed cobalt nanoparticles, giving it a significant activity. This thesis extends the study of the liquid-assisted mechanochemical approach to M-N-C type catalyst synthesis, in which iron is used as the doping metal.

# 2 THE AIMS OF THE THESIS

- Aim #1 To explore the present-day research on the topic.
- Aim #2 To investigate the underlying processes of oxygen reduction reaction and oxygen evolution reaction.
- Aim #3 To understand the basics of measurement techniques and methods featured in the thesis.
- Aim #4 To develop a sustainable synthetic protocol for production of efficient bi-functional catalyst of Fe-N-C type.
- Aim #5 To describe the created catalyst material by various physical characteristic techniques.
- Aim #6 To perform electrochemical tests in order to define oxygen reduction and evolution reaction kinetic parameters.
- Aim #7 To compare the obtained electrochemical activities across the sample series.
- Aim #8 To examine the suitability of the most efficient sample for practical application in Zn-air battery device.
- Aim #9 To link the elucidated structural features and composition to the presented ORR, OER, and bifunctional performance values.

# 3 EXPERIMENTAL PART

## 3.1 MATERIALS AND METHODS

### 3.1.1 Chemicals and Materials

2,4,6-tri(2-pyridyl)-1,3,5-triazine (tripyridyl triazine – TPTZ, ≥98%, Sigma-Aldrich), ferric chloride ($FeCl_3$, Sigma-Aldrich), hydrochloric acid (HCl), ethyl alcohol (EtOH). Sodium chloride (NaCl) - pulverized in a ball mill to achieve an average crystallite size of 10–50 µm. 2 – propanol (isopropyl alcohol, IPA), potassium hydroxide (KOH) Nafion perfluorinated resin solution (5 wt%, Sigma-Aldrich), commercial PtRu (Pt – 50 wt%, Ru – 25 wt%) on high surface area carbon support (Thermo Scientific). Ultrapure water (18.2 MΩ cm; Milli-Q purification system by Millipore) was used to prepare all solutions.

### 3.1.2 Catalyst Synthesis

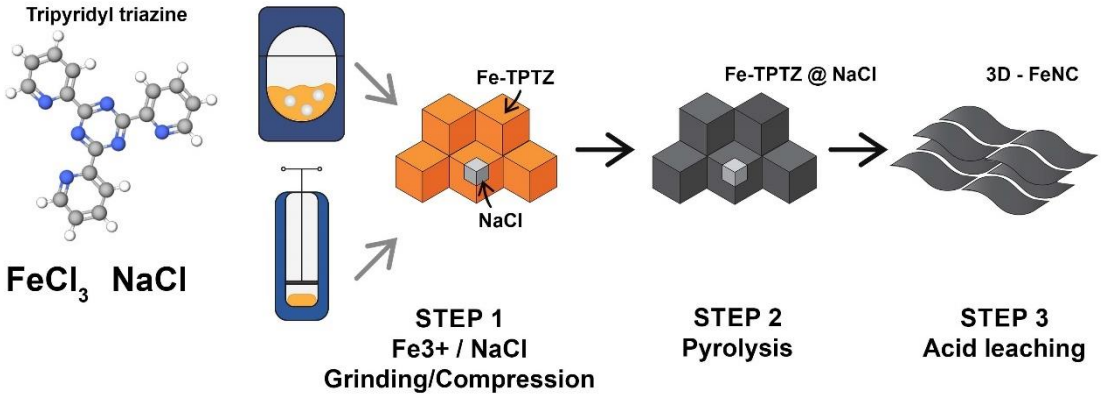


Figure 2. Schematic illustration of steps of catalyst synthesis via liquid-assisted grinding and liquid-assisted compression.

The schematics of the catalyst preparation can be seen in Fig. 2. The general approach of catalyst synthesis is green mechanochemical production of Fe-N-C complex using salt 'template' to achieve sheets of graphene-like structure.

**F1P:** In order to synthesize template-free catalyst via liquid-assisted grinding, 100 mg (0.32 mmol, 3 eq.) of 2,4,6-tri(2-pyridyl)-1,3,5-triazine (TPTZ), 17.3 mg (0.11 mmol, 1 eq) of $FeCl_3$ and 40 µL of EtOH were ground in a ball mill at 600 rpm for 20 min. Then, the calcination process was carried out at 800 °C for 1 h with a heating rate of 50 °C $min^{-1}$ under $N_2$.

Chemical etching was also employed to remove excess metal or oxide compounds using 1 M HCl at 70 °C for 3 h. The final mass of the F1P sample was m=23.6 mg.

**F2P:** For synthesizing the template-mediated catalyst via liquid assisted grinding, 100 mg (0.32 mmol, 3 eq.) of 2,4,6-tri(2-pyridyl)-1,3,5-triazine (TPTZ), 17.3 mg (0.11 mmol, 1 eq) of $FeCl_3$, 1000 mg of NaCl and 40 µL of EtOH were ground in a ball mill at 600 rpm for 20 min. Then, the calcination process was carried out at 800 °C for 1 h with a heating rate of 50 °C $min^{-1}$ under $N_2$. NaCl was washed out with MilliQ water. Chemical etching was also employed to remove excess metal or oxide compounds using 1 M HCl at 70 °C for 3 h. The final mass of the F2P sample was m=39.8 mg.

**F3P:** To synthesize template-mediated catalyst via liquid assisted compression, 100 mg (0.32 mmol, 3 eq.) of 2,4,6-tri(2-pyridyl)-1,3,5-triazine (TPTZ), 17.3 mg (0.11 mmol, 1 eq) of $FeCl_3$, 1000 mg of NaCl were fully mixed and poured into a pellet mold. Then 40 µL of EtOH was added. Materials were compressed using the pressure of 300 kg $cm^{-2}$ (≈294.2 bar). Afterward, the calcination process was carried out at 800 °C for 1 h with a heating rate of 50°C $min^{-1}$ under $N_2$. NaCl was washed out with MilliQ water. Chemical etching was also employed to remove excess metal or oxide compounds using 1 M HCl at 70°C for 3 h. The final mass of the F3P sample was m=40.0 mg.

Milling was conducted in a ball mill (Fritsch Planetary Mill Pulverisette 7) using 12 mL zirconium oxide grinding bowls and 5 mm diameter zirconium oxide milling balls. Furnace (Carbolite Gero EST 12/300B) was used to carbonize catalyst precursors.

### 3.1.3 Physical characterization

*Nitrogen physisorption measurements*

$N_2$ adsorption-desorption isotherms were analyzed at the temperature T = -196 °C (boiling point of $N_2$) using NovaTouch LX2 (Quantachrome Instruments). Before the analysis, the samples underwent a vacuum drying process for 12 h at a temperature of T = 300 °C. From nitrogen isotherms, the specific surface area (SBET) of carbon samples was calculated with the assumption of the Brunauer–Emmett–Teller (BET) theory in the interval P/P0 = 0.02–0.2. The formula APS = 2Vtot/SBET was used to calculate the average pore size with the pores assumed to be slit-type. The quenched solid density functional theory (QSDFT) equilibrium model for slit-type pores was used to calculate the pore size distribution (PSD). The software TouchWin 1.11 (Quantachrome Instruments) was used to perform all calculations.

*X-Ray Photoelectron Spectroscopy (XPS)*

A non-monochromatic twin anode X-ray tube (Thermo XR3E2) and an electron energy analyzer (SCIENTA SES 100) were used for X-ray photoelectron spectroscopy. The characteristic energy of an X-ray tube was 1253.6 eV (Mg Kα). Parameters of the survey scan were the following: energy range – from 900 to 0 eV, pass energy – 200 eV, step size – 0.5 eV, duration – 0.2 s, and the number of scans – 5. High-resolution XPS was conducted, setting the pass energy to 200 eV and the step size to 0.1 eV. The energy reference for the measurements was a silver wire on the sample holders (Ag 3d5/2 at 367.8 eV). Charging effects were not detected. CasaXPS (version 2.3.16) software was employed to complete the peak fitting using Gauss–Lorentz hybrid function (GL 70, Gauss: Lorentz = 30%: 70%) with a mix of Shirley-type and linear backgrounds. Sample preparation included deposition on the glassy carbon plates (dimensions: 1.1 × 1.1 cm) of the catalysts suspended in isopropyl alcohol (concentration, 4 mg $mL^{-1}$).

*Powder X-Ray Diffraction (PXRD)*

PXRD was performed with Bruker D8 Advance diffractometer using Ni-filtered CuKα radiation, two 2.5° Soller slits, 0.3° divergence slit, and the LynxEye line detector. The total counting time was set to 174 s per step, scanning steps – 0.013°2θ from 5 to 77°2θ.

*Microwave Plasma Atomic Emission Spectroscopy (MP-AES)*

MP-AES was used to analyze the concentration of metals in the bulk of the catalysts. The analysis was performed with Agilent 4210 MP-AES. Analytical wavelengths were set to Fe 371.993 nm and Co 340.512 nm. Microwave digestion (Anton Paar Multiwave PRO system) was utilized for sample preparation to dissolve the catalyst materials (10 mg each) in a mixture of 2 mL of $H_2O_2$ and 4 mL of $HNO_3$ in NXF100 vessels (PTFE/TFM liner). Digestion parameters were the following: temperature – 230 °C, pressures in the range of 45 and 50 bar. Afterward, dilution to 5 mg $L^{-1}$ of metal concentration was carried out with 2% $HNO_3$.

*Scanning electron microscopy (SEM)*

SEM analysis of the catalysts was performed to determine the structure. A high-resolution SEM-FIB electron microscope, Helios 5 UX (FEI-Thermo Scientific), was employed for SEM measurements to reveal the morphology of the carbon-based structures and the nanoparticles. The microscope was used at 30 kV with STEM 3+ BF and HAADF detectors. For SEM, holey carbon film grid S147-4 (Agar Scientific) was utilized for sample transfer.

### 3.1.4 Electrochemical characterization

*Ink Preparation*

The catalyst ink for electrode modification was prepared by sonicating 5 mg of catalyst material, 5 μL of Nafion ionomer solution (5 wt%, Sigma-Aldrich), and 495 μL of IPA for 20 min to obtain a uniform ink.

*Electrode modification*

For electrode preparation, Teflon embedded glassy carbon (GC) disk was polished with 0.3 μm alumina slurry (Buehler). To remove the alumina remnants, the electrode was cleaned in Milli-Q water and isopropyl alcohol in an ultrasonic bath for 5 min. Afterward, it was quickly rinsed with water and dried to remove any moisture.

The catalyst suspension was dropped onto the GC area with five 2 μL steps (10 μL in total) to achieve a material loading of 0.5 mg $cm^{-2}$. After this, the electrode was dried in an oven at 60 °C for 1-2 minutes and then air-dried for at least 10 min.

*Electrochemical measurements*

The electrochemical catalytic activity of the materials was evaluated with the typical three-electrode, five-neck cell system connected to the Autolab PGSTAT128N potentiostat/galvanostat (Metrohm Autolab B.V., The Netherlands) and controlled by Nova 2.1.4 software. The glassy carbon rotating disk electrode (OrigaTip: GC disk, diameter - 5 mm, area, normalized - 0.2 $cm^2$), silver-silver chloride (Ag/AgCl) electrode, and a platinum rod were used as a working electrode, a reference electrode, and a counter electrode respectively. The alkaline electrolyte solution was prepared via dissolution of 2.8 g of KOH (purity ≥99.998%, Sigma-Aldrich) in 500 mL of Milli-Q water. The electrolyte was then saturated either with pure O2 (99.999%, Linde Gas) or deaerated with Ar gas (99.999%, Linde Gas).

The cyclic voltammetry (CV) curves and the background correction curves were obtained in Ar-saturated electrolyte at 50 mV $s^{-1}$ and 10 mV $s^{-1}$ scan rates, respectively. The samples were also subjected to CV in an Ar-saturated solution to determine the electrochemical double-layer capacitance. The loaded electrode was cycled through the 10, 20, 30, 40, and 50 mV $s^{-1}$ scan rates. Points of cathodic and anodic current densities were extracted from the measured data at non-Faradaic potentials with values ranging from 1.05 V to 1.25 V (vs. RHE). The records were taken of the ORR polarization curves in $O_2$-saturated 0.1 M KOH

electrolyte with the scan rate of 10 mV $s^{-1}$ and various rotation speeds (namely 360, 610, 960, 1600, 1900, 3100). Then, the OER activity in Ar-saturated electrolyte (0.1 M KOH) was investigated with the scan rate set to 10 mV $s^{-1}$. 85% iR compensation was applied to all electrochemical data where required. Potentials were then converted to RHE with the formula: $E_{Ag/AgCl} = E_{RHE} - 0.966$ ($E_{vs\ RHE} = E_{vs.Ag/AgCl} + 0.0591*pH + E_{Ag/AgCl}^{\theta}$ (0.209)).

The main kinetic parameters of ORR were extracted from polarization curves. These parameters were onset and half-wave potentials ($E_{onset}$ and $E_{1/2}$), kinetic current density ($j_k$), diffusion-limited current density ($j_d$), number of electrons transferred per oxygen molecule, and Tafel slope. The RDE data was analyzed by the Koutecky–Levich (K–L) equation:

$$\frac{1}{j} = \frac{1}{j_k} + \frac{1}{j_d} = \frac{1}{nFkC_{O_2}^b} + \frac{1}{0.62nFC_{O_2}^b D_{O_2}^{2/3} \upsilon^{-1/6} \omega^{1/2}}$$

The current densities (mA $cm^{-2}$) in the above equation are j - measured current density, $j_k$ - kinetic current density, and $j_d$ – diffusion-limited current density. The remaining values are defined as follows: ω is the electrode rotation rate (rad $s^{-1}$), n is the electron transfer number per oxygen molecule, F is the Faraday constant (96 485 C $mol^{-1}$) [45], $C^b_{O2}$ is the oxygen concentration in 0.1 M KOH ($1.2 \times 10^{-6}$ mol $cm^{-3}$), $D_{O2}$ is the diffusion coefficient of $O_2$ ($1.9 \times 10^{-5}$ $cm^2$ $s^{-1}$ in 0.1 M KOH), and υ – kinematic viscosity of the solution (0.01 $cm^2$ $s^{-1}$) [46].

The overall oxygen electrode bifunctional activity was calculated as the potential difference (ΔE) at an ORR at the half-wave potential ($E_{1/2}$) and an OER current density of 10 mA $cm^{-2}$ ($E_{j=10}$): $\Delta E = E_{j=10} - E_{1/2}$.

*Assembly of Zn-air battery*

The in-house Zn-air battery (ZAB) tests were tested with a single-cell battery in a two-electrode configuration. The air cathode with a geometric area of 3.5 $cm^2$ was constructed from a nickel mesh, which acts as a current collector, and a carbon paper, which serves as a gas diffusion layer (Sigracet BB39). This layer was coated in F2P catalyst ink (loading of 2 mg $cm^{-2}$) by drop-casting and then spread by a hand brush coating technique to achieve an even layer. Zn foil (99%) and 6 M KOH solution were utilized as an anode and electrolyte, respectively. The catalyst ink for the ZAB was prepared by sonicating 7 mg of F2P electrocatalyst, 20 μl of 5% Nafion ionomer solution (SigmaAldrich), 0.2 mL of MilliQ water, and 0.6

mL of ethanol for 1.5 h. The preparation of benchmark PtRu catalyst ink was done in the same manner.

The battery cell was constructed as a set of stacked plates in the following order: a bottom plate with the anode, a center plate for the electrolyte, a filling neck, a cathode, and a top plate containing a 1.8 cm air duct for airflow. Generally, keeping a hermetic environment between anode and cathode is necessary to avoid any electrolyte leakage. Galvanostatic tests were controlled by a potentiostat (AUTOLAB PGSTAT204).

## 3.2 RESULTS AND DISCUSSION

### 3.2.1 Synthesis

Organic molecules are often used as precursors for M-N-C type materials for confirming the presence of carbon and nitrogen in appropriate amounts in the catalyst [47]. Herein, 2,4,6-tris(2-pyridyl)-1,3,5- triazine (TPTZ) was used as a carbon/nitrogen source and a ligand to form Fe-TPTZ complexes. Coordinative bonding between the metals and nitrogen in M-TPTZ materials results in a formation of numerous M-Nx sites, which have displayed promising electrocatalytic activities [41], [46], [48], [49]. TPTZ molecules were also found to stabilize metal ions and prevent their clustering in M-TPTZ complexes [41], [48], [49]. Moreover, the sodium chloride template used for the synthesis of the F2P, and F3P could stabilize Fe-TPTZ complexes during heat annealing process, which would expose catalytically active sites and significantly improve the porosity [50]. Comparatively coarser NaCl crystals could also help in the milling process by reducing the particle size and in-creasing the material dispersion [51].

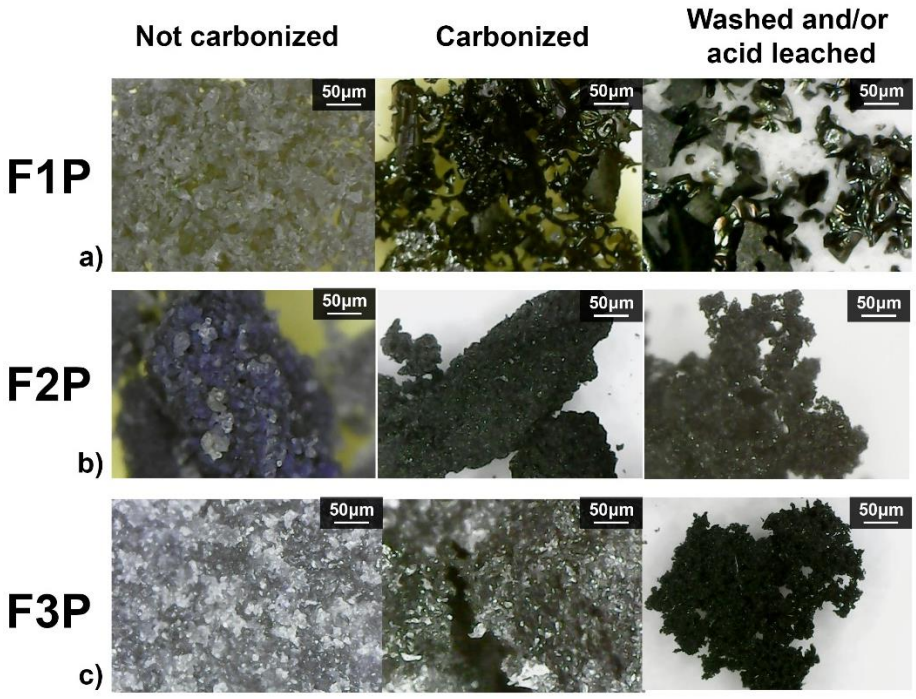


Figure 3. Captured microscope images of (a) F1P, (b) F2P, and (c) F3P materials at various stages of synthesis.

Microscopy images of pre-carbonized catalysts in Fig. 3b, 3c show uniform incorporation of fine NaCl particles that facilitate the Fe-TPTZ framework creation. After the heat treatment,

the salt crystals are visibly incorporated into the carbon matrix for the NaCl-supported materials. On the other hand, the F1P sample (Fig. 3a), synthesized without sodium chloride, does not demonstrate these inclusions. Before the acid leaching, F2P and F3P samples first require the removal of NaCl. After the heat treatment, the images show that F1P appears as solid pieces of carbon, while the F2P and F3P samples demonstrate uniform and porous macrostructure. Therefore, the stabilization effect of the carbonization has a significant impact, as represented by the differences between the F1P, F2P, and F3P samples. In fact, the stabilization is preserved even during the mechanochemical synthesis, which goes beyond the referenced wet-chemistry synthesis protocols.

While the mentioned template-assisted procedures provide efficient catalysts, they usually involve wet-chemistry methods and a complicated workup. Therefore, the solid-state mechanochemical approaches could make catalyst synthesis procedure more sustainable and cost-effective [41], [50]. The implementation of this process results in three times less time and energy spent, as concluded by Kosimov et al. [43], who report a similar synthesis protocol.

### 3.2.2 Physical characterization

***SEM***

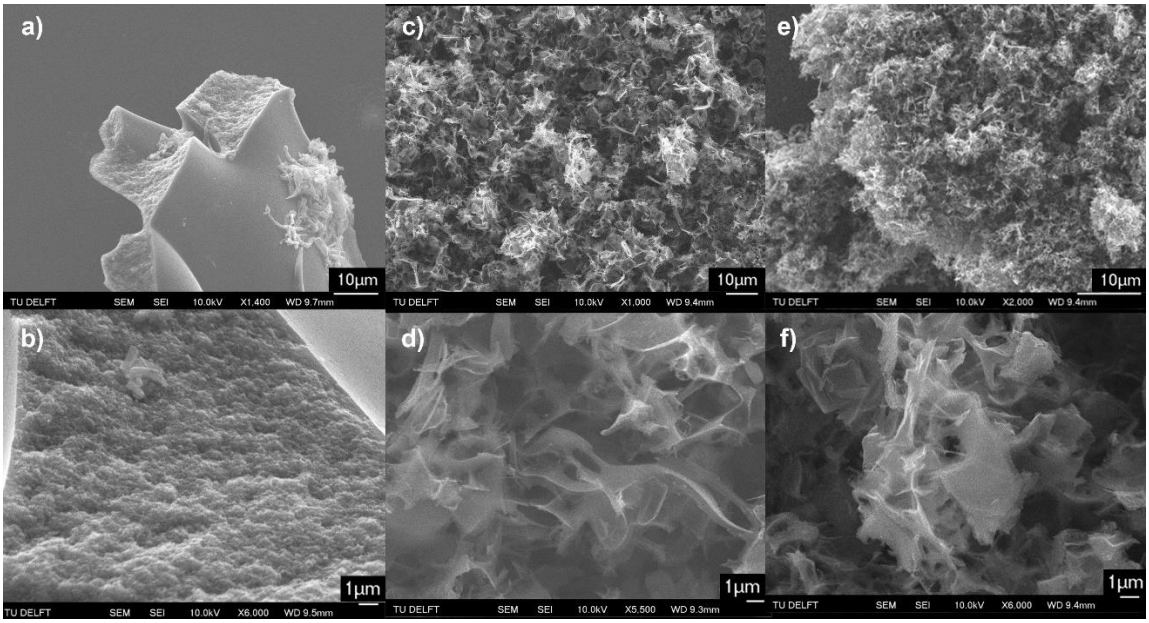


Figure 4. SEM images of (a,b) F1P catalyst, (c,d) F2P catalyst, and (e,f) F3P catalyst at different magnifications.

Scanning electron microscopy was performed to determine the microstructure of the catalyst materials (Fig. 4). The F1P catalyst, synthesized without a NaCl template, exhibits a dense

and tightly arranged structure. The rest of the electrocatalysts, on the other hand, are considerably looser. Overall, the microstructures of F2P and F3P can be described as interconnected sheet-like crumpled planes. F3P, which is prepared via compression, exhibits a little more closely packed smaller fragments of the material. Conversely, F2P, prepared by grinding, shows a lightly packed matrix. These images suggest that the template-assisted synthesis dramatically facilitates the creation of sparsely organized structures, allowing for active sites to be more accessible.

***XPS***

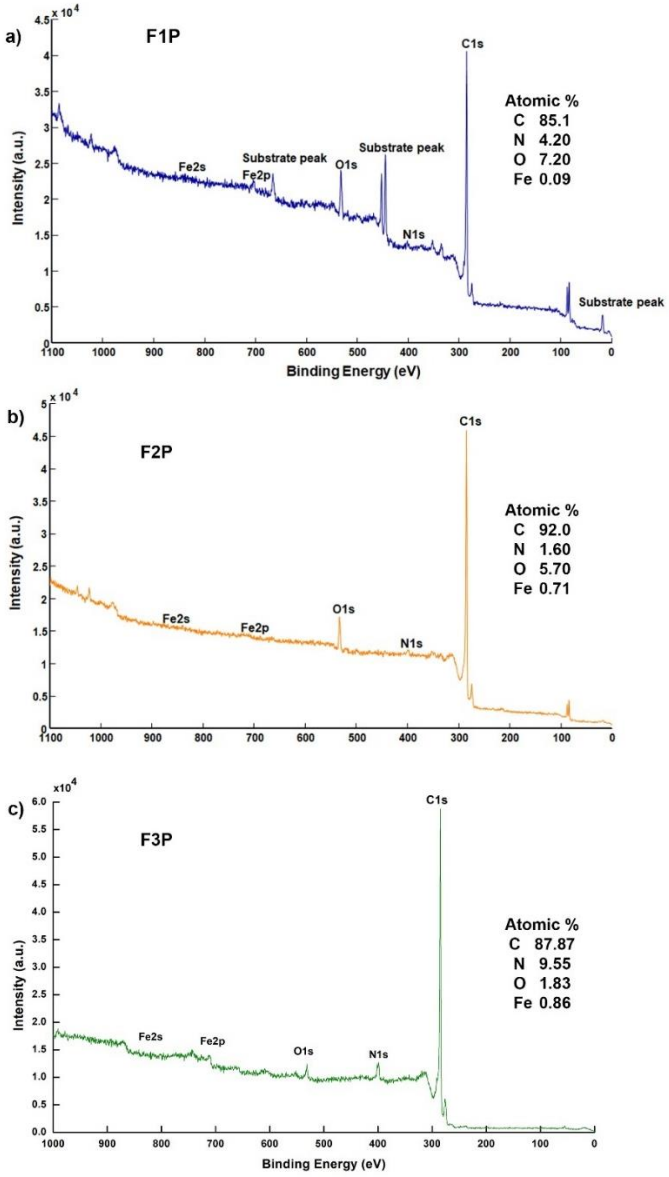


Figure 5. XPS survey spectra of (a) F1P, (b) F2P, and (c) F3P catalysts.

X-ray photoelectron spectroscopy was used to study the surface morphology of Fe-N-C catalysts. It can be seen from the survey spectra (Fig. 5) that the surface of synthesized samples

contains iron, carbon, nitrogen, and oxygen species. The peaks across samples are indexed to C 1s, N 1s, O 1s, and Fe 2s, 2p. To attribute the bonding of the species, these peaks must be deconvoluted. Surface elemental content analysis for F1P, F2P, and F3P is presented in Fig. 5. Overall, F1P contains significantly smaller amounts of nitrogen and iron species. This can potentially result in an inferior electrochemical activity compared to the other samples. The F2P sample is composed of 92 at.% of C, 1.60 at.% of N, 5.70 at.% of O, and 0.71 at.% of Fe, which appear to have a satisfactory content for bifunctional activity. However, F3P exhibits a significantly larger share of nitrogen (9.55 at.%) and iron (0.86 at.%), which increases the likelihood of Fe-$N_x$ sites. These could make the F3P catalyst highly favorable to the ORR/OER activity [52]–[54].

***MP-AES***

The material's elemental composition was assessed with the MP-AES technique. As the samples were dissolved and then excited with the external energy source (microwave plasma), the atoms exhibited distinctive spectra (i.e., they emit radiation in particular patterns). The target metals analyzed in the catalysts were iron, sodium, zirconium, and cobalt. The largest share of iron, about 9.3 % by weight (Table 1), was detected in the F3P sample. Such value might be caused by the preparation method of this catalyst, as its compression led to a denser packing of the material and bulkier clusters of iron, which are difficult to wash out during etching.

Since NaCl was used as a template for some samples during the preparation process, the samples were analyzed for sodium remnants. Here, F1P demonstrated the smallest value – 0.002 wt.%. This was expected, as no sodium chloride was used in its synthesis. On the other hand, F2P and F3P displayed 0.089 and 0.319 wt.% of Na, respectively. The larger share of sodium in the F3P sample may be caused by factors explained above (i.e., iron discussion). The source of Zr traces in the samples was the milling process. In fact, no measurable values of zirconium were found in F1P, while F2P and F3P showed small but detectable amounts. This could be because salt was ball-milled using a zirconium oxide bowl and balls only for F2P and F3P. However, Zr impurities caused by liquid-assisted grinding are likely insignificant, as F1P does not show traceable amounts. Negligible cobalt traces in F2P and F3P were attributed to the impurity in the iron salt used in the synthesis. Overall, these trace amounts of Na, Zr, and Co metals were too small to influence the bifunctional electrocatalytic properties of the samples.

Table 1. Bulk metal composition of metals (wt.%) determined from MP-AES analysis.

| Catalyst | Bulk metal composition (wt.%) | | | |
|---|---|---|---|---|
| | Fe | Na | Zr | Co |
| F1P | 0.960 | 0.002 | – | – |
| F2P | 1.471 | 0.089 | 0.011 | 0.003 |
| F3P | 9.276 | 0.319 | 0.009 | 0.031 |

***XRD***

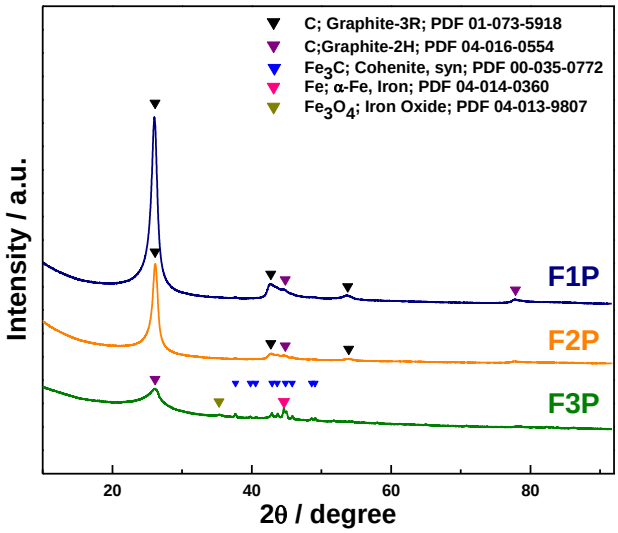


Figure 6. XRD patterns of the samples F1P, F2P, and F3P.

The crystal structure of the catalyst materials F1P, F2P, and F3P were analyzed by powder X-ray diffraction method (Fig. 6). A peak belonging to the (002) plane can be observed at 26º, which hints at a graphitic morphology of the materials [38]. Notably, the rather intensive peaks correspond to the rhombohedral (3R) graphite (Graphite – 3R) for F1P and F2P, while the less prominent peak – is to the hexagonal structure (Graphite – 2H) of F3P. The lower intensity of this characteristic carbon peak represents a lower degree of graphitization [55]. F1P and F2P samples also show peaks at 44.5º that correspond to the 2H phase of graphite. Overall, F1P and F2P, prepared by grinding, show diffraction peaks at the same 2θ values for 3R (42.5º, 54.6º) and 2H (44.3º, 77.7º) peaks. However, these curves show no apparent peaks related to any of the iron species (elemental, oxide, carbide). This might signify that

iron is evenly dispersed atomically [56]. In contrast, compression prepared F3P exhibits one peak related to elemental iron (α-Fe) at 44.3º and iron oxide ($Fe_3O_4$) at 35.5º, as well as a collection of peaks related to iron carbide species ($Fe_3C$) from 39º to 45º. These results indicate the presence of the Fe clusters in the catalyst [57]. In addition, while the formation of less active metal-based species (Fe/$Fe_3C$) inevitably suggests a lower amount of more active F-$N_x$ sites, the Fe/$Fe_3C$ species can still contribute to F3P ORR activity by a stepwise $2e^- \times 2e^-$ manner forming the peroxides and then decomposing them to water [53], [58].

### *$N_2$ physisorption*

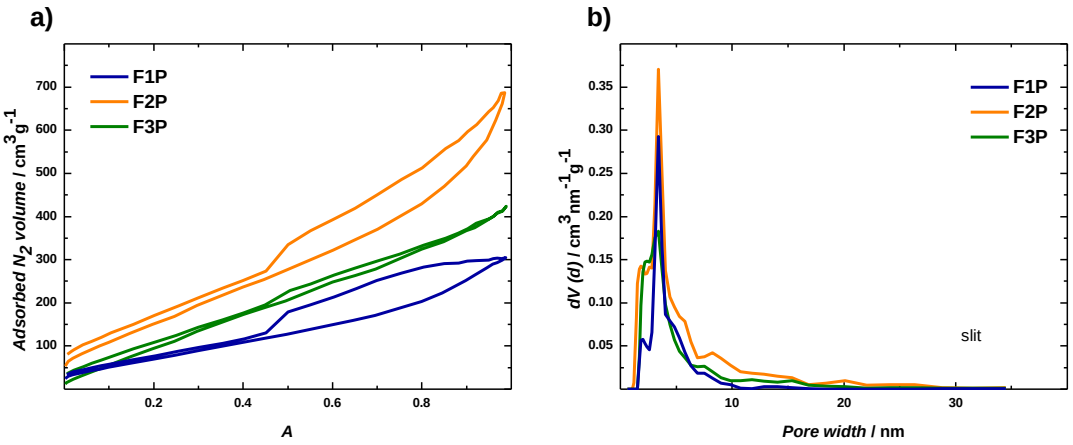


Figure 7. (a) Nitrogen adsorption-desorption isotherms; (b) Pore size distribution curves.

To characterize the porosity and specific surface area of the material, nitrogen gas adsorption and desorption analysis was used. The adsorption-desorption isotherms in Fig. 7a. exhibit Type IV hysteresis loop shape, which implies the presence of micro- and mesopores. The quenched solid density functional theory (QSDFT) equilibrium model (Fig. 7b.) was applied to identify the pore size distribution. As such, micropores and mesopores were primarily distributed over the range of 1.2 – 2 nm and 2 – 34 nm, respectively. The values of the specific surface area of the materials were obtained by BET (Brunauer−Emmett−Teller) analysis (Table 2). Among the samples, F2P has the largest $S_{BET}$ = 563 $m^2 g^{-1}$, while F1P and F3P show values of 269 $m^2 g^{-1}$ and 430 $m^2 g^{-1}$, respectively. The specific methods of preparation can cause these differences in surface area. Correlation between surface area and total pore volume is also noticeable, with F2P having the largest pore volume of 0.97 $cm^3 g^{-1}$, followed by F3P – 0.63 $cm^3 g^{-1}$ and F1P – 0.46 $cm^3 g^{-1}$. Average pore radii were calculated to be 3.42 nm, 3.45 nm, and 2.93 nm for F1P, F2P, and F3P, respectively. The analysis allows us to conclude that these materials were of composite nature, containing a mixture of

micro- and mesoporous structures. This bears great importance on charge and mass transfer in catalysis.

Table 2. Specific surface area, total pore volume, and average pore size of the catalyst materials were determined from $N_2$ physisorption analysis.

| Sample | BET surface area ($S_{BET}$ / $m^2$ $g^{-1}$ ) | Total pore volume ($cm^3$ $g^{-1}$ ) | Average pore size (nm) |
|---|---|---|---|
| F1P | 269 | 0.46 | 3.42 |
| F2P | 563 | 0.97 | 3.45 |
| F3P | 430 | 0.63 | 2.93 |

### 3.2.3 Electrochemical characterization

#### *Cyclic voltammetry tests*

Initially, cyclic voltammetry (CV) tests of FxP samples were completed in 0.1 M KOH Ar-saturated electrolyte at 50 mV $s^{-1}$ (Fig. 8). The CV curve does not show any characteristic redox peaks for the F1P sample. On the contrary, both F2P and F3P show broad oxidation peaks centering around 0.29 V, which might be due to the contribution from the redox of the $Fe^0/Fe^{2+}$ couple [59]. Moreover, F3P at 0.6 V exhibits weak oxidation and reduction peaks of quinone/hydroquinone at the surface. Even though a quasi-rectangular profile can be seen in Fig 8. for all the measured samples, the capacitive layer for F1P is far smaller compared to F2P and F3P, implying the presence of a smaller double-layer capacitance (DLC) [60].

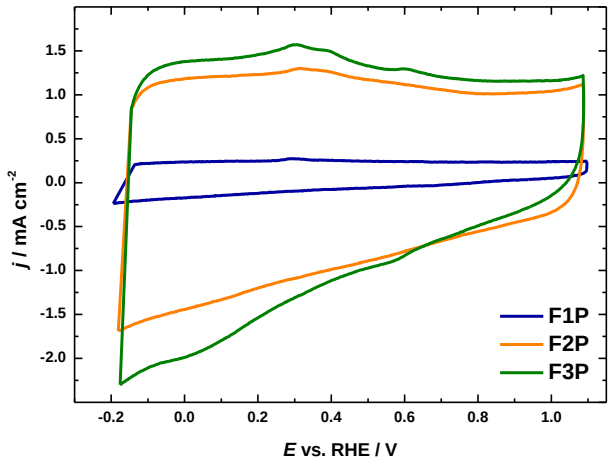


Figure 8. Cyclic voltammetry curves for the catalysts at the scan rate of 50 mV $s^{-1}$ in Ar-saturated solution.

This can be further verified and extended with electrochemical active surface area (ECSA) measurements. The surface area of catalysts can be quantified by electrochemically measuring the double layer capacitance with different scan rates using the CV technique [61]. The scan rate and DLC are linearly dependent on the current density in which no Faradaic processes occur (i.e., charging current density, $j_c$). Its values are calculated from CV measurements and are presented as a function of scan rates. Afterward, the trendline is then fitted through the points. The slope of this line is essentially the $C_{DL}$ (double layer capacitance) since the relation $j_c = \upsilon C_{DL}$ is valid [62].

The average cathodic and anodic current density values were obtained from the cyclic voltammograms of FxP catalysts (Fig 9a, 9c, 9e.) at 1.15 V vs. RHE. The charging current density is then an absolute value of the cathodic and anodic current density values: $j_c = |j_{cath} - j_{anod}|$. The calculated points were plotted against the scan rates, and the slope values were 2.7 mF $cm^{-2}$, 21.3 mF $cm^{-2}$, 21.0 mF $cm^{-2}$ for F1P, F2P and F3P respectively (Fig. 9b, 9d, 9f). It is important to note that the double layer capacitance was given for $cm^2$ of the geometric area, so the values should be multiplied by the electrode area ($S_{electrode}$ = 0.196 $cm^2$) to get F1P $C_{DL}$ = 0.529 mF, F2P $C_{DL}$ = 4.175 mF, and F3P $C_{DL}$ = 4.116 mF.

The ECSA of catalyst samples was determined with the equation $ECSA = \frac{C_{DL}}{C_s}$, where $C_s$ is the specific capacitance of the ideal flat surface of the catalyst under the same electrolyte conditions. For the FxP materials, the specific capacitance was selected to be Cs = 0.040 mF $cm^{-2}$ based on the commonly reported value [62], [63]. The ECSA values are then 13.2 $cm^2$

for F1P, 104.4 $cm^2$ for F2P, and 102.7 $cm^2$ for F3P. Therefore, the F2P catalyst shows the biggest surface area, while the F1P shows the smallest. A similar trend can be noticed in BET measurements of the surface area.

Overall, the ECSA method has limitations as specific capacitance is valid only empirically. As such, the value of $C_s$ for the synthesized catalysts is usually approximated due to various challenges in the calculating process [61]. In general, most methods for geometric area determination come with certain issues. BET technique, for example, is limited by the gas molecule size and accessibility of the catalyst surface [64].

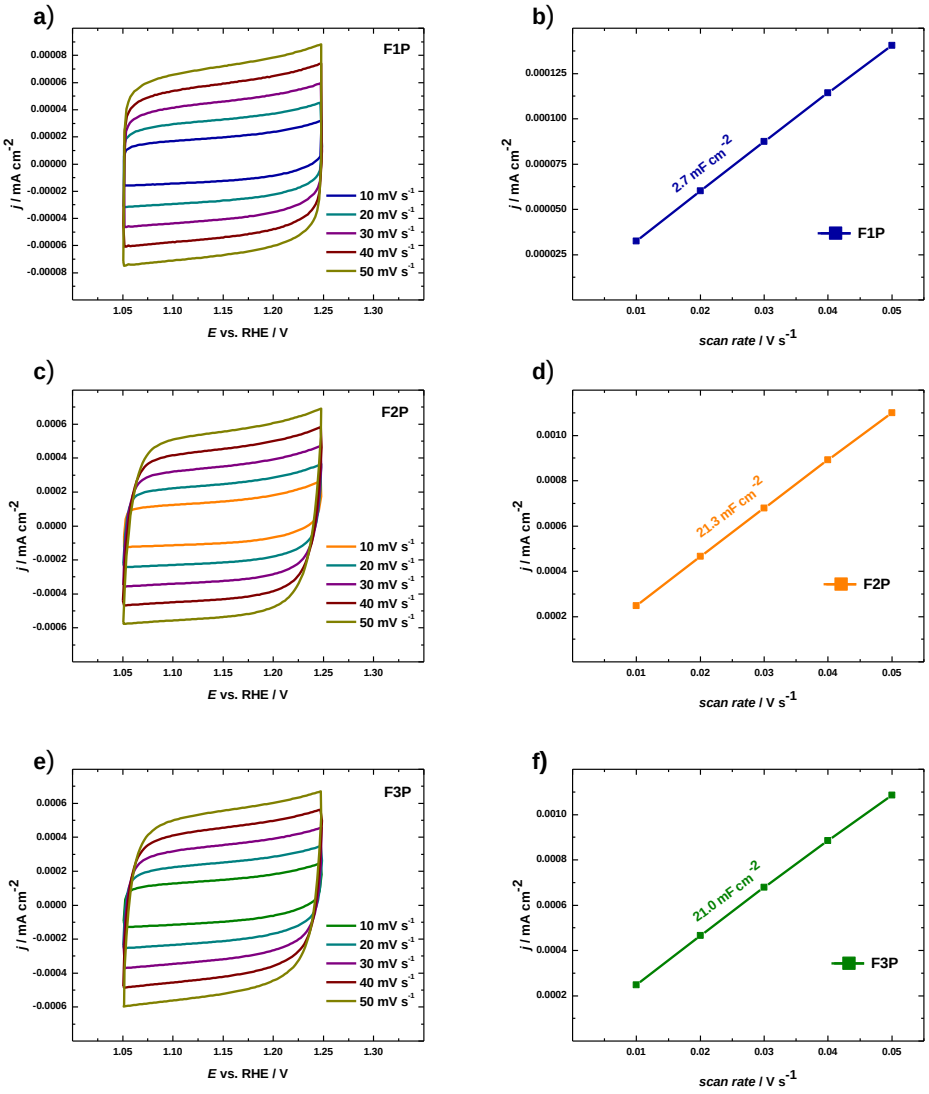


Figure 9. Double-layer capacitance measurements for evaluation of the electrochemical surface area. Non-Faradeic CV scans of F1P (a), F2P (c), and F3P (e) at various scan rates; the charging current densities plotted against the scan rates for the F1P (b), F2P (d), F3P (f) respectively.

### *Rotating disc electrode tests*

To examine the ability of the prepared materials to act as bifunctional catalysts for ORR/OER rotating disk electrode (RDE) studies of FxP samples were performed in an alkaline (0.1 M KOH) medium in $O_2$-saturated environment. ORR polarization curve was measured at 1600 rpm and was corrected by subtracting the background current. The background current was recorded in an $O_2$-free electrolyte solution.

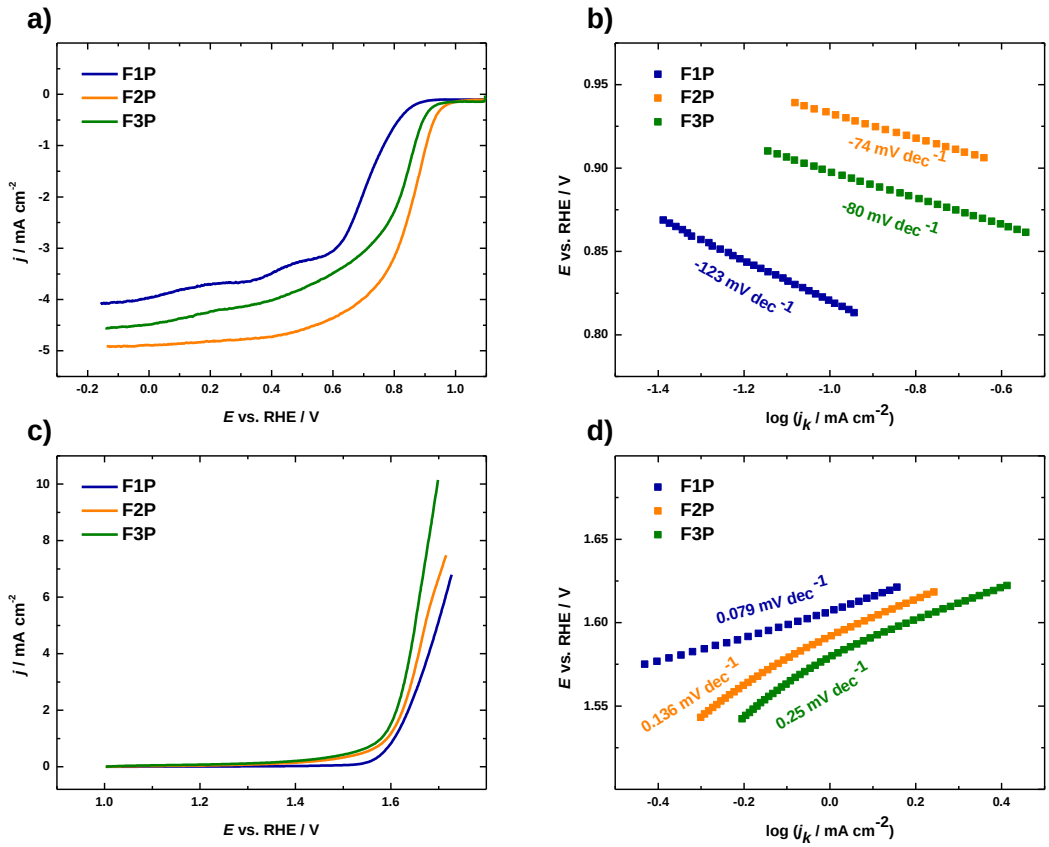


Figure 10. (a) Comparison of ORR polarization curves of FxP samples obtained at 1600 rpm in $O_2$-saturated 0.1 M KOH solution; (b) Tafel plots constructed from the RDE data; (c) comparison of the OER activity of different samples in Ar-saturated electrolyte; (d) corresponding Tafel plots constructed from the OER data.

The F2P catalyst displays the best electrochemical ORR catalytic activity with an onset potential $E_{on}$ = 1.00 V and a half-wave potential $E_{1/2}$ = 0.85 V. Values of onset and half-wave potentials for F1P and F3P can be seen in the Table 3 and comparison of polarization curves in Fig. 10. Notably, F2P shows a better activity not only in terms of potentials but also in terms of limiting current densities in the diffusion-controlled region, as the values of current densities tend to be more negative. The difference in electrocatalytic properties corresponds

to the efficient electron- and mass- transfer, which is caused by higher porosity and abundance of accessible pyridinic-N and Fe-N-C sites [38], [39]. Catalyst F3P prepared by compression shows the second-best result in activity towards ORR. This may be attributed to the higher concentration of Fe sites, which was also confirmed by XRD.

Table 3. Summary of electrochemical performance characteristics of the catalyst samples.

| **Sample** | $E_{1/2}$ **(V)** | $E_{on}$ **(V)** | ***n*** | $E_{j=10}$ **OER (V)** | $\eta_{OER}$ **(V)** | $\Delta E$ **(V)** |
|---|---|---|---|---|---|---|
| F1P | 0.69 | 0.89 | 3.24 | 1.78 | 0.55 | 1.09 |
| F2P | 0.85 | 1.00 | 3.85 | 1.75 | 0.52 | 0.90 |
| F3P | 0.80 | 0.94 | 3.81 | 1.70 | 0.47 | 0.90 |

To understand the kinetics of the ORR, a Tafel analysis was conducted (Fig. 10b). Tafel slope values were −123, −74, and −80 mV $dec^{-1}$ for F1P, F2P, and F3P, respectively. The effectiveness of the F2P as a catalyst can also be explained by the smallest absolute value of the Tafel slope among the measured. In general, a smaller absolute Tafel slope corresponds to the faster kinetics. Polarization curves were also measured at rotation rates of 360, 610, 960, 1900, and 3100 rpm to elucidate the oxygen reduction reaction pathways. The Koutecky–Levich (K-L) plots were constructed from the gathered data. First-order reaction kinetics of ORR with respect to the concentration of dissolved $O_2$ were observed from the K-L plots with good parallelism and linearity. The ORR pathway is interpreted from the electron transfer number calculated from the K-L equation. The electron transfer number (n) for samples F1P, F2P, and F3P can be seen in Table 3 and an insets on Fig. 11b,d and f. For F2P and F3P, the value of n is closer to four, suggesting primarily the $4e^-$ pathway that leads to water formation.

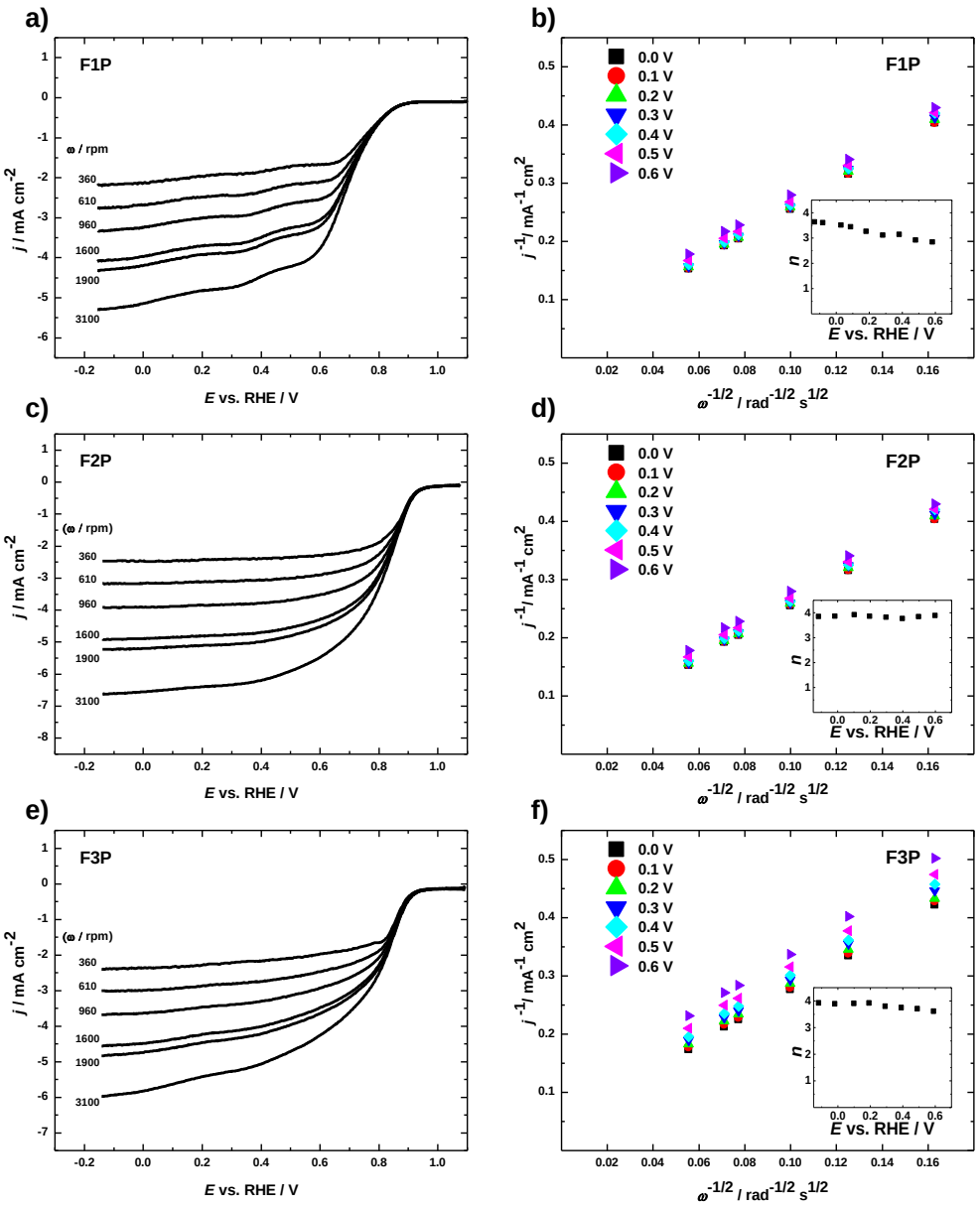


Figure 11. (a, c, e) RDE polarization curves at different rotation speeds of modified GC electrodes measured in $O_2$-saturated electrolyte solution (0.1M KOH); (b, d, f) K-L plots of corresponding samples. Inset graphs: number of electrons transferred per oxygen molecule.

In order to further investigate the bifunctionality, OER measurements were employed. The electrodes were scanned in 0.1 M KOH under an Ar-saturated environment at 1600 rpm in the 1-1.8 V (vs. RHE). The results are displayed in Table 3. As shown in Fig. 10c, the potential needed to reach a current density of 10 mA $cm^{-2}$ ($E_{j=10}$) is 1.70 V for F3P, 1.72 V for F2P, and 1.74 V for F1P. Among the samples, F3P proved to perform better in OER. The Tafel plots of the samples in Fig 10d show slopes of 0.079, 0.136, and 0.25 mV $dec^{-1}$ for

F1P, F2P, and F3P, respectively, suggesting more favorable OER kinetics for the F2P catalyst. From the presented catalysts, the most efficient bifunctionality (ΔE = 0.90 V) is exhibited by F2P and F3P samples (Fig. 12).

The characterization analyses results indicate that both the porosity of the material and density of Fe-$N_x$ sites are essential contributors to the efficient bifunctionality. With a large number of active sites, the catalyst needs to have a sufficient porosity to maintain a well-wetted surface. A less porous structure would decrease the wetting of the total surface, leaving a large share of reaction sites unreachable and thus inactive [65]. For electrocatalytic materials, a larger surface area is also beneficial for reaching a higher current density with lower overpotential. In addition, improved porosity promotes the migration of oxygen molecules and other reactants, which in turn corresponds to increased mass diffusion [66]. Therefore, the F2P sample was chosen to further test the applicability of the synthesized catalysts.

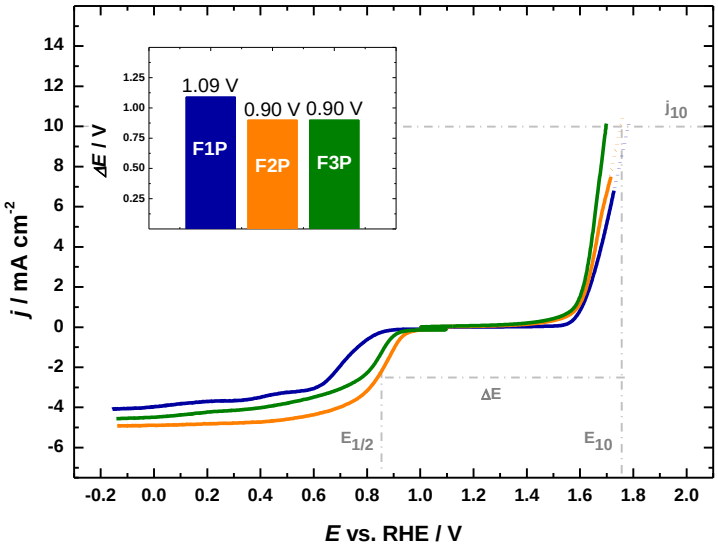


Figure 12. The overall electrocatalytic activity of the F1P, F2P, and F3P samples. Lines represent the following values: $E_{1/2}$ represents the halfwave potential for ORR, $j_{10}$ – current density that equals 10 mA $cm^{-2}$, $E_{10}$ – potential at the current density $j_{10}$ (10 mA $cm^{-2}$), ΔE – the potential difference; inset: the ΔE of the samples.

Table 4 reports the activity of the recently reported Fe-N-C type bifunctional catalysts that have been synthesized via wet-chemistry methods. It can be observed that the best performing catalysts produced and characterized in this thesis (F2P and F3P) are quite comparable to those referenced. However, the described protocol has significant advantages: minimal

amounts of non-toxic solvents, inexpensive and available chemicals, short reaction time, and a straightforward protocol. These result in small to no toxic waste and less time, energy, and resources spent on the catalyst production.

Table 4. A summary of electrochemical parameters and the respective specific surface values of the recently published articles reporting on Fe-N-C type catalyst mater.

| **Catalyst Name, Reference** | **Precursors** | **Specific surface area ($m^2$ $g^{-1}$)** | **ORR (0.1 M KOH)** | | | **OER (0.1 M KOH)** | **$\Delta E = E_{j=10} - E_{1/2}$** |
|---|---|---|---|---|---|---|---|
| | | | **$E_{onset}$ (vs. RHE)** | **$E_{1/2}$ (vs. RHE)** | **Electron number, n** | **$E_j$=10** | |
| Fe-N-C900, [38] | 2,6-Diacetylpyridine, 1,8-Diaminonaphthalene, Iron(III) chloride hexahydrate. | 1,795.68 | 1.09 V | 0.908 V | 3.98 | 1.61 V | 0.702 V |
| Fe-N-C, [40] | N, N-dimethylformamide, 2-aminoterephthalic acid, iron (III) chloride; | 593.0 | 0.985 V | 0.872 V | 3.65 | 1.753 V | 0.881 V |
| SAC-FeN-WPC, [39] | Dried eucalyptus wood, FeCl3·6H2O, NH3 gas (during pyrolysis) | 1183.23 | 0.99 V | 0.85 V | 3.9 – 4.0 | 1.64 V | 0.79 V |
| FeNxial synthesis-embedded PNC, [55] | Graphene, polypyrrole, 2, 2-bipyridine, iron chloride | 1161.56 | 0.997 V | 0.86 V | 4 | 1.635 V | 0.775 V |
| FeImid-800, [67] | Ferrocene, imidazole | 289 | 0.90 V | 0.81 V | 3.93 – 3.95 | 1.81 V | 1.00 V |
| Fe7C3@ FeNC, [68] | Iron chloride, ellagic acid, melamine | 236 | 0.96 V | 0.83 V | 2.8 | 1.62 V | 0.79 V |
| Fe–N–NDC-1-900, [56] | Phthalocyanine iron, 2-Aminoterephthalic acid, N,N-dimethylformamide | 346.4 | 1.06 V | 0.89 V | 3.92 | 1.58 V | 0.69 V |

| | | | | | | | |
|---|---|---|---|---|---|---|---|
| Fe–N–C/2rGO, [57] | Reduced graphene oxide, $Fe(NO_3)_3 \cdot 9H_2O$, 2-methylimidazole | 571 | 0.99 V | 0.88 V | 3.9 | 1.56 V | 0.69 V |
| Fe—N—Csyn, [60] | Hexamethylenetetramine, $Fe(NO_3)_3$, sucrose, polyvinylpyrrolidone | 380.4 | 0.87 V | 0.63 V | 3.92 – 4.02 | 1.70 V | 1.07 V |
| Fe-NC/rOCNT, [69] | Oxidized carbon nanotubes, polyvinyl pyrrolidone, tris(acetylacetonato) iron(III), 2-methylimidazole | 233.4 | 0.865 V | 0.982 V | 4.0 | 1.789 V | 0.807 V |

### 3.2.4 Zn-Air Battery Performances

To further explore the practical utilization of the most promising material (F2P), a Zn-air battery was constructed and analyzed in-house (Fig. 13a,b). Charge-discharge polarization curve (Fig. 13c) exhibits an open voltage of 1.3 V, which is quite close to the value of the reference material (PtRu). It can be seen from the graph that the maximal power density of F2P (132 mW $cm^{-2}$) is slightly lower compared to the benchmark PtRu material (139 mW $cm^{-2}$).

In addition, cycling tests were performed to assess the long-term application of the catalyst material at the air cathode. The galvanostatic charge-discharge cycling measurement was run at the current density of 5 mA $cm^{-2}$. The overall voltage-time profile in Fig. 14a shows drastic fluctuations in cell potential at certain points, which may be attributed to the instability of the system as dendrites form. At these points, the battery was disconnected to refresh the electrolyte solution and the metallic (Zn) electrode. The ’imperfect’ stepwise shape of the cycles, which are especially obvious for the charging peaks (Fig 14b), can be explained by dendrites causing internal short circuits [70].

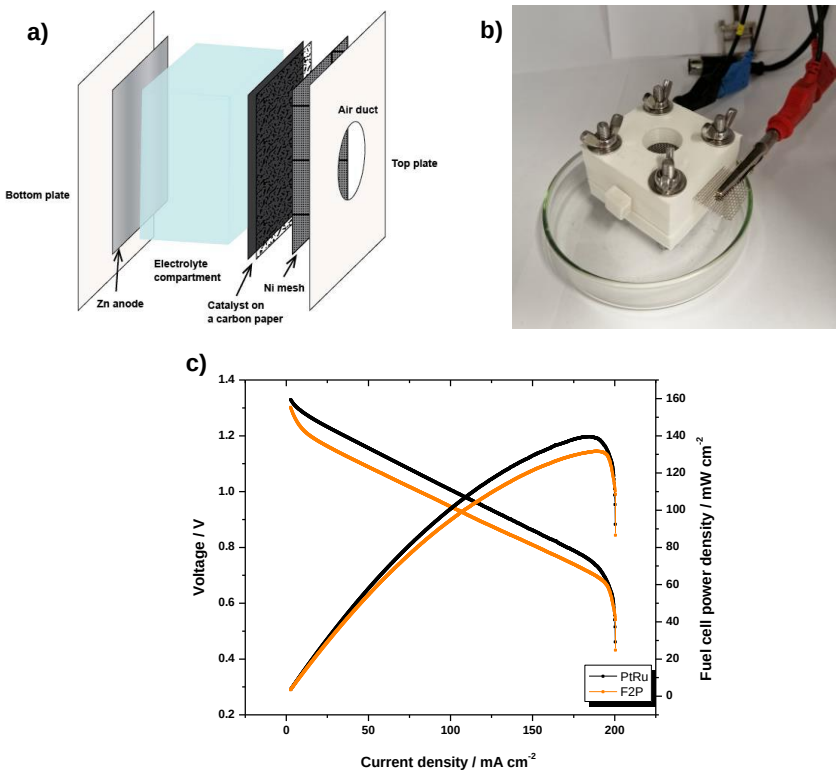


Figure 13. (a) A schematic illustration of a battery constructed for the ZAB tests; (b) a photo of the constructed ZAB; (c) Power density curves of F2P and PtRu as catalysts on the air cathode.

Generally, dendrites form under particular conditions coupled with electrochemical processes at the electrodes and cause instability of the battery [71]. The formation of dendrites can be reduced by electrolyte modification (e.g., the addition of an organic modifier) or updating the anode design (e.g., increasing a specific surface area) [72]. Furthermore, the subsequent cycles show better stability, as the voltage gap difference between the beginning and end of the last cycle is significantly smaller than the first (Fig. 14c and Fig. 14d). In addition, comparing the length of the cycles in-between the "refreshment" times shows that most of the cycles are quite long while the initial cycle is considerably shorter. Thus, the first cycle can be viewed as a 'stabilization' run, during which the material is activated and stabilized. The activated catalyst then performs more efficiently and shows a more even and more prolonged run. Overall, the cycling of PtRu (Fig. 14a) exhibits inferior stability, as its total cycling profile and runs at the 'refreshment' intervals are significantly shorter compared to the F2P. Moreover, the closing cycle of PtRu demonstrates considerable fluctuations, which makes F2P a better catalyst for a zinc-air battery.

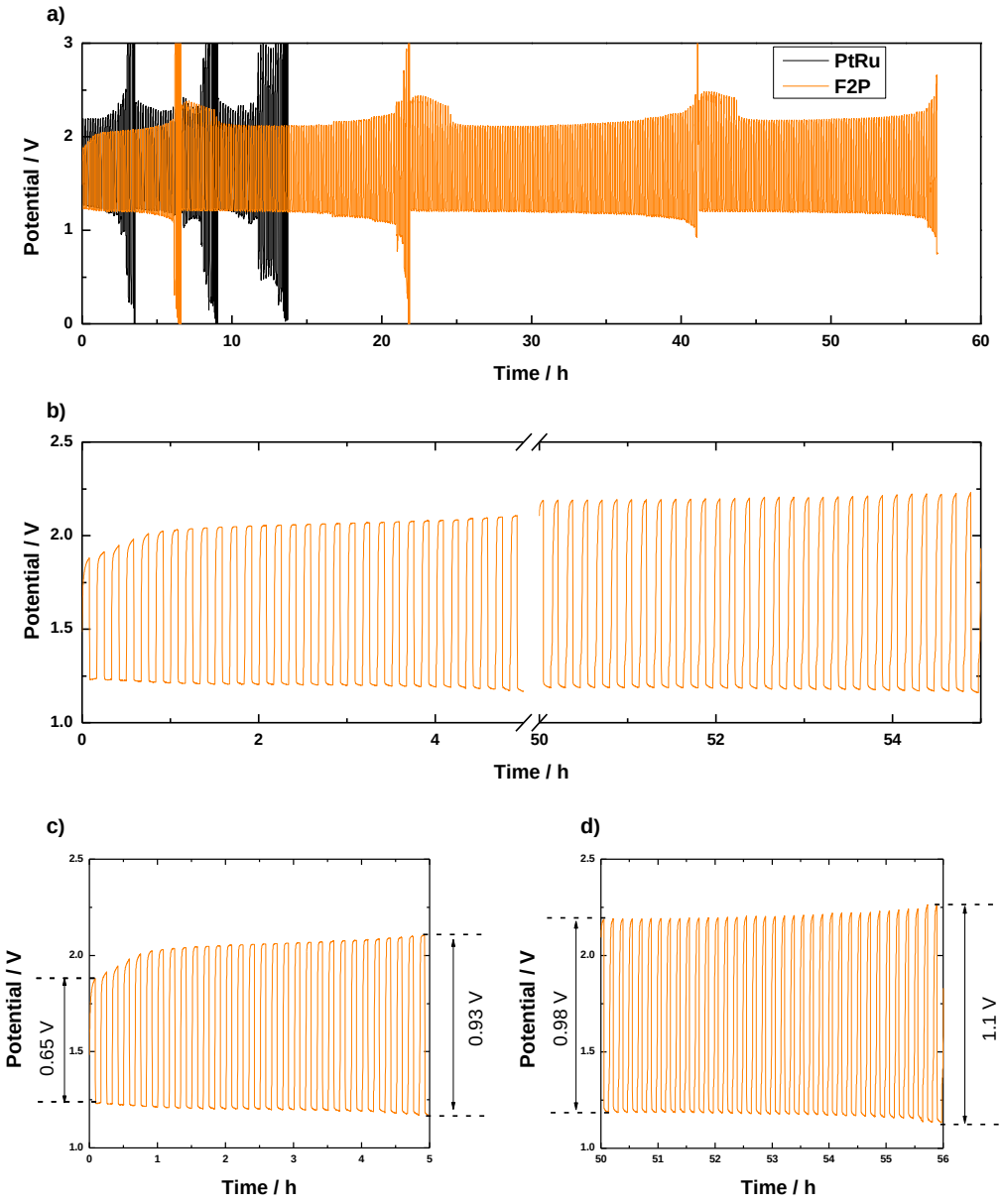


Figure 14. (a) Galvanostatic charging/discharging cycling curves on F2P and PtRu materials (in orange and black respectively) performed at 5 mA $cm^{-2}$; (b) F2P charging/discharging curve reduced to first and the last cycle; (c) The first cycle and (d) the final cycle with noted voltage gap difference values at the beginning and the end of the corresponding cycle.

## SUMMARY

The work describes an original Fe-N-C type catalyst synthesis that is favorable both environmentally and economically. The excellent bifunctional activity was obtained by mechanochemical reaction completed through LAG and LAC of tripyridyl triazine and iron (III) chloride precursors. SEM imaging shows interconnected nanosheets of template-assisted F2P and F3P samples. Furthermore, $N_2$ physisorption and BET analysis results indicate that the incorporation of sodium chloride crystals as a template significantly improved the porosity of the catalysts. Specifically, the template-free F1P showed the lowest BET surface area values and denser microstructure, as shown by SEM. From a synthesis point of view, the sodium chloride template greatly enhances the porosity necessary for efficient ORR and OER, while ball grinding ensures evenly distributed iron throughout the catalyst bulk. Additionally, F1P and F2P revealed a higher degree of graphitization of carbon than F3P through XRD analysis. The latter catalyst also contains clusters of iron species within its structure, while XRD patterns of F1P and F2P suggest the presence of atomical dispersion of iron.

The activity of F1P, F2P, and F3P samples was studied by CV and RDE tests. Expectedly, less porous F1P showed inferior activity towards the ORR/OER. On the other hand, F2P exhibited higher $E_{1/2}$ and $E_{onset}$ (0.85 V and 1.00 V, respectively), and F3P was more favorable towards OER ($E_{j=10}$ = 1.70 V). Both F2P and F3P show a $4e^-$ ORR pathway. The bifunctional activity described by a potential difference ($\Delta E$) was equal between F2P and F3P (0.90 V). The efficiency of F2P and F3P materials towards ORR/OER can be attributed to more significant amounts of nitrogen and iron in the carbon matrix. As confirmed by XPS, F3P contains considerably larger quantities of nitrogen and iron, leading to its high OER activity. As the bifunctional activity of F3P is equal to F2P, it can be concluded that not only the Fe-$N_x$ sites secure good activity but also the porosity (higher for F2P).

The functionality of F2P was tested in the Zn-air battery. The ZAB studies showed a slightly smaller F2P maximal power density than the reference PtRu material (132 mW $cm^{-2}$ vs. 139 mW $cm^{-2}$, respectively). However, the F2P catalyst is considerably more stable than its discussed counterpart, as represented by charge-discharge cycling tests.

These results illustrate the effectiveness of a novel method that is straightforward, scalable, and sustainable for prospective large-scale production of catalyst material for metal-air batteries.

## ACKNOWLEDGEMENTS

I would like to express my gratitude to Dr. Nadezda Kongi for supervising, supporting, and guiding provided throughout my laboratory experience and thesis writing.

I would like to thank MSc. Akmal Kosimov (UT) for the prepared sample, Also, I would like to credit the concept and experiment design to him.

I would like to thank MSc. Gulnara Yusibova (UT) for immense help in the laboratory and mentoring me in this project.

I would like to thank BSc. Jürgen-Martin Assafrei (UT) for Zn-air battery measurements.

Also, I would like to extend my appreciation to Dr. Maike Käärik (UT) for the $N_2$ physisorption measurements and subsequent calculations, to Dr. Jaan Aruväli (UT) for the XRD measurement, to Dr. Päärn Paiste (UT) for the MP-AES measurements, and Dr. Arvo Kikas (UT) for XPS analysis.

# REFERENCES


[1] Yana Popkostova, "EUROPE'S ENERGY CRISIS CONUNDRUM Origins, impact and way forward," *European Union Institute for Security Studies*, Jan. 2022. [Online]. Available: https://www.iss.europa.eu/content/europes-energy-crisis-conundrum

[2] H. Ibrahim, A. Ilinca, and J. Perron, "Energy storage systems—Characteristics and comparisons," *Renew. Sustain. Energy Rev.*, vol. 12, no. 5, pp. 1221–1250, Jun. 2008, doi: 10.1016/j.rser.2007.01.023.

[3] A. P. Amrute, J. De Bellis, M. Felderhoff, and F. Schüth, "Mechanochemical Synthesis of Catalytic Materials," *Chem. – Eur. J.*, vol. 27, no. 23, pp. 6819–6847, Apr. 2021, doi: 10.1002/chem.202004583.

[4] "REPowerEU: Joint European action for more affordable, secure and sustainable energy," Mar. 08, 2022. https://ec.europa.eu/commission/presscorner/detail/en/ip_22_1511 (accessed Mar. 09, 2022).

[5] "Factsheet - REPowerEU: Joint European action for more affordable, secure and sustainable energy." European Union, Mar. 2022. doi: 10.2775/076377.

[6] C. Ponce de León, A. Frías-Ferrer, J. González-García, D. A. Szánto, and F. C. Walsh, "Redox flow cells for energy conversion," *J. Power Sources*, vol. 160, no. 1, pp. 716–732, Sep. 2006, doi: 10.1016/j.jpowsour.2006.02.095.

[7] B. Dunn, H. Kamath, and J.-M. Tarascon, "Electrical Energy Storage for the Grid: A Battery of Choices," *Science*, vol. 334, no. 6058, pp. 928–935, Nov. 2011, doi: 10.1126/science.1212741.

[8] J. Z. Vladimir Neburchilov, *Metal-Air Batteries and Metal-Sulfur Batteries: Fundamentals and Applications*, 1st edition. CRC Press, 2016.

[9] M. Winter and R. J. Brodd, "What Are Batteries, Fuel Cells, and Supercapacitors?," *Chem. Rev.*, vol. 104, no. 10, pp. 4245–4270, Oct. 2004, doi: 10.1021/cr020730k.

[10] Q. Liu, Z. Pan, E. Wang, L. An, and G. Sun, "Aqueous metal-air batteries: Fundamentals and applications," *Energy Storage Mater.*, vol. 27, pp. 478–505, May 2020, doi: 10.1016/j.ensm.2019.12.011.

[11] J. Z. Vladimir Neburchilov, *Metal-Air Batteries and Metal-Sulfur Batteries: Fundamentals and Applications*, 1st edition. CRC Press, 2016.

[12] Q. Liu, Z. Pan, E. Wang, L. An, and G. Sun, "Aqueous metal-air batteries: Fundamentals and applications," *Energy Storage Mater.*, vol. 27, pp. 478–505, May 2020, doi: 10.1016/j.ensm.2019.12.011.

[13] Y. Li and J. Lu, "Metal–Air Batteries: Will They Be the Future Electrochemical Energy Storage Device of Choice?," *ACS Energy Lett.*, vol. 2, no. 6, pp. 1370–1377, Jun. 2017, doi: 10.1021/acsenergylett.7b00119.

[14] L. Chen, X. Xu, W. Yang, and J. Jia, "Recent advances in carbon-based electrocatalysts for oxygen reduction reaction," *Chin. Chem. Lett.*, vol. 31, no. 3, pp. 626–634, Mar. 2020, doi: 10.1016/j.cclet.2019.08.008.

[15] C. Lei *et al.*, "Nanostructured Carbon Based Heterogeneous Electrocatalysts for Oxygen Evolution Reaction in Alkaline Media," *ChemCatChem*, vol. 11, no. 24, pp. 5855–5874, Dec. 2019, doi: 10.1002/cctc.201901707.

[16] X. Wu, C. Tang, Y. Cheng, X. Min, S. P. Jiang, and S. Wang, "Bifunctional Catalysts for Reversible Oxygen Evolution Reaction and Oxygen Reduction Reaction," *Chem. – Eur. J.*, vol. 26, no. 18, pp. 3906–3929, Mar. 2020, doi: 10.1002/chem.201905346.

[17] R. Ma *et al.*, "A review of oxygen reduction mechanisms for metal-free carbon-based electrocatalysts," *Npj Comput. Mater.*, vol. 5, no. 1, p. 78, Dec. 2019, doi: 10.1038/s41524-019-0210-3.

[18] M. Rana, S. Mondal, L. Sahoo, K. Chatterjee, P. E. Karthik, and U. K. Gautam, "Emerging Materials in Heterogeneous Electrocatalysis Involving Oxygen for Energy Harvesting," *ACS Appl. Mater. Interfaces*, vol. 10, no. 40, pp. 33737–33767, Oct. 2018, doi: 10.1021/acsami.8b09024.
[19] S. Divanis, T. Kutlusoy, I. M. Ingmer Boye, I. C. Man, and J. Rossmeisl, "Oxygen evolution reaction: a perspective on a decade of atomic scale simulations," *Chem. Sci.*, vol. 11, no. 11, pp. 2943–2950, 2020, doi: 10.1039/C9SC05897D.
[20] J. M. Gonçalves, T. A. Matias, K. C. F. Toledo, and K. Araki, "Electrocatalytic materials design for oxygen evolution reaction," in *Advances in Inorganic Chemistry*, vol. 74, Elsevier, 2019, pp. 241–303. doi: 10.1016/bs.adioch.2019.03.002.
[21] Z. Ahmed and V. Bagchi, "Current trends and perspectives on emerging Fe-derived noble-metal-free oxygen electrocatalysts," *New J. Chem.*, vol. 45, no. 47, pp. 22012–22033, 2021, doi: 10.1039/D1NJ05062A.
[22] S.-E. Jang and H. Kim, "Effect of Water Electrolysis Catalysts on Carbon Corrosion in Polymer Electrolyte Membrane Fuel Cells," *J. Am. Chem. Soc.*, vol. 132, no. 42, pp. 14700–14701, Oct. 2010, doi: 10.1021/ja104672n.
[23] E. Antolini, "Iridium As Catalyst and Cocatalyst for Oxygen Evolution/Reduction in Acidic Polymer Electrolyte Membrane Electrolyzers and Fuel Cells," *ACS Catal.*, vol. 4, no. 5, pp. 1426–1440, May 2014, doi: 10.1021/cs4011875.
[24] K. R. Yoon, G. Y. Lee, J.-W. Jung, N.-H. Kim, S. O. Kim, and I.-D. Kim, "One-Dimensional $RuO_2$/$Mn_2O_3$ Hollow Architectures as Efficient Bifunctional Catalysts for Lithium–Oxygen Batteries," *Nano Lett.*, vol. 16, no. 3, pp. 2076–2083, Mar. 2016, doi: 10.1021/acs.nanolett.6b00185.
[25] J. Pan *et al.*, "Recent Progress on Transition Metal Oxides as Bifunctional Catalysts for Lithium-Air and Zinc-Air Batteries," *Batter. Supercaps*, vol. 2, no. 4, pp. 336–347, Apr. 2019, doi: 10.1002/batt.201800082.
[26] J. Wang *et al.*, "Earth-abundant transition-metal-based bifunctional catalysts for overall electrochemical water splitting: A review," *J. Alloys Compd.*, vol. 819, p. 153346, Apr. 2020, doi: 10.1016/j.jallcom.2019.153346.
[27] H. Wang, M. Zhou, P. Choudhury, and H. Luo, "Perovskite oxides as bifunctional oxygen electrocatalysts for oxygen evolution/reduction reactions – A mini review," *Appl. Mater. Today*, vol. 16, pp. 56–71, Sep. 2019, doi: 10.1016/j.apmt.2019.05.004.
[28] R. Khan *et al.*, "Role of perovskites as a bi-functional catalyst for electrochemical water splitting: A review," *Int. J. Energy Res.*, vol. 44, no. 12, pp. 9714–9747, Oct. 2020, doi: 10.1002/er.5635.
[29] L. Yang, X. Zeng, W. Wang, and D. Cao, "Recent Progress in MOF-Derived, Heteroatom-Doped Porous Carbons as Highly Efficient Electrocatalysts for Oxygen Reduction Reaction in Fuel Cells," *Adv. Funct. Mater.*, vol. 28, no. 7, p. 1704537, Feb. 2018, doi: 10.1002/adfm.201704537.
[30] D. Liu, Y. Tong, X. Yan, J. Liang, and S. X. Dou, "Recent Advances in Carbon-Based Bifunctional Oxygen Catalysts for Zinc-Air Batteries," *Batter. Supercaps*, vol. 2, no. 9, pp. 743–765, Sep. 2019, doi: 10.1002/batt.201900052.
[31] R. Cepitis, N. Kongi, V. Grozovski, V. Ivaništšev, and E. Lust, "Multifunctional Electrocatalysis on Single-Site Metal Catalysts: A Computational Perspective," *Catalysts*, vol. 11, no. 10, p. 1165, Sep. 2021, doi: 10.3390/catal11101165.
[32] Y. Cheng, J. Zhang, and S. P. Jiang, "Are metal-free pristine carbon nanotubes electrocatalytically active?," *Chem. Commun.*, vol. 51, no. 72, pp. 13764–13767, 2015, doi: 10.1039/C5CC02218E.
[33] W. Ding *et al.*, "Space-Confinement-Induced Synthesis of Pyridinic- and Pyrrolic-Nitrogen-Doped Graphene for the Catalysis of Oxygen Reduction," *Angew. Chem. Int. Ed.*, vol. 52, no. 45, pp. 11755–11759, Nov. 2013, doi: 10.1002/anie.201303924.

[34] Y. Wang, Z. Tang, S. Shen, and J. Yang, “The influence of heteroatom doping on the performance of carbon-based electrocatalysts for oxygen evolution reactions,” *New Carbon Mater.*, vol. 37, no. 2, pp. 321–336, Apr. 2022, doi: 10.1016/S1872-5805(22)60591-2.
[35] Y. Wang *et al.*, “Metal–Nitrogen–Carbon Catalysts of Specifically Coordinated Configurations toward Typical Electrochemical Redox Reactions,” *Adv. Mater.*, vol. 33, no. 34, p. 2100997, Aug. 2021, doi: 10.1002/adma.202100997.
[36] R. Jasinski, “A New Fuel Cell Cathode Catalyst,” *Nature*, vol. 201, no. 4925, pp. 1212–1213, Mar. 1964, doi: 10.1038/2011212a0.
[37] S. Gupta, D. Tryk, I. Bae, W. Aldred, and E. Yeager, “Heat-treated polyacrylonitrile-based catalysts for oxygen electroreduction,” *J. Appl. Electrochem.*, vol. 19, no. 1, pp. 19–27, Jan. 1989, doi: 10.1007/BF01039385.
[38] D. Lyu *et al.*, “Ultra-high surface area graphitic Fe-N-C nanospheres with single-atom iron sites as highly efficient non-precious metal bifunctional catalysts towards oxygen redox reactions,” *J. Catal.*, vol. 368, pp. 279–290, Dec. 2018, doi: 10.1016/j.jcat.2018.10.025.
[39] L. Zhong *et al.*, “Wood Carbon Based Single-Atom Catalyst for Rechargeable Zn–Air Batteries,” *ACS Energy Lett.*, vol. 6, no. 10, pp. 3624–3633, Oct. 2021, doi: 10.1021/acsenergylett.1c01678.
[40] X. Zhang, X. Hu, S. Lv, Y. Li, J. Ren, and Y. Huang, “Hollow NH2-MIL-101@TA derived electrocatalyst for enhanced oxygen reduction reaction and oxygen evolution reaction,” *Int. J. Hydrog. Energy*, vol. 46, no. 78, pp. 38692–38700, Nov. 2021, doi: 10.1016/j.ijhydene.2021.09.107.
[41] C. Guo *et al.*, “Molten-salt/oxalate mediating Fe and N-doped mesoporous carbon sheet nanostructures towards highly efficient and durable oxygen reduction electrocatalysis,” *Microporous Mesoporous Mater.*, vol. 303, p. 110281, Aug. 2020, doi: 10.1016/j.micromeso.2020.110281.
[42] T. Friščić, A. V. Trask, W. Jones, and W. D. S. Motherwell, “Screening for Inclusion Compounds and Systematic Construction of Three-Component Solids by Liquid-Assisted Grinding,” *Angew. Chem. Int. Ed.*, vol. 45, no. 45, pp. 7546–7550, Nov. 2006, doi: 10.1002/anie.200603235.
[43] A. V. Trask and W. Jones, “Crystal Engineering of Organic Cocrystals by the Solid-State Grinding Approach,” in *Organic Solid State Reactions*, vol. 254, F. Toda, Ed. Berlin, Heidelberg: Springer Berlin Heidelberg, 2005, pp. 41–70. doi: 10.1007/b100995.
[44] A. Kosimov *et al.*, “Liquid-assisted grinding/compression: a facile mechanosynthetic route for the production of high-performing Co–N–C electrocatalyst materials,” *Green Chem.*, vol. 24, no. 1, pp. 305–314, 2022, doi: 10.1039/D1GC03433B.
[45] E. R. Cohen and B. N. Taylor, “The 1986 adjustment of the fundamental physical constants,” *Rev. Mod. Phys.*, vol. 59, no. 4, pp. 1121–1148, Oct. 1987, doi: 10.1103/RevModPhys.59.1121.
[46] J. Wu, Z. Meng, R. Zhang, T. Tian, R. Wang, and H. Tang, “Boosting Oxygen Reduction Catalysis with Hierarchically Porous Fe-Doped Carbon by Chemical Vapor Deposition in Zn–Air Batteries,” *Energy Fuels*, vol. 36, no. 7, pp. 4006–4014, Apr. 2022, doi: 10.1021/acs.energyfuels.2c00099.
[47] L. Osmieri, A. H. A. Monteverde Videla, and S. Specchia, “The use of different types of reduced graphene oxide in the preparation of Fe-N-C electrocatalysts: capacitive behavior and oxygen reduction reaction activity in alkaline medium,” *J. Solid State Electrochem.*, vol. 20, no. 12, pp. 3507–3523, Dec. 2016, doi: 10.1007/s10008-016-3332-2.

[48] H. Hadadzadeh, M. Maghami, J. Simpson, A. D. Khalaji, and K. Abdi, “Nickel(II) polypyridyl Complexes of 2,4,6-Tris(2-pyridyl)-1,3,5-triazine,” *J. Chem. Crystallogr.*, vol. 42, no. 7, pp. 656–667, Jul. 2012, doi: 10.1007/s10870-012-0296-7.
[49] P. Paul, B. Tyagi, A. K. Bilakhiya, M. M. Bhadbhade, E. Suresh, and G. Ramachandraiah, “Synthesis and Characterization of Rhodium Complexes Containing 2,4,6-Tris(2-pyridyl)-1,3,5-triazine and Its Metal-Promoted Hydrolytic Products: Potential Uses of the New Complexes in Electrocatalytic Reduction of Carbon Dioxide,” *Inorg. Chem.*, vol. 37, no. 22, pp. 5733–5742, Nov. 1998, doi: 10.1021/ic9709739.
[50] C. Guo *et al.*, “Boosting the oxygen reduction activity of a three-dimensional network Co–N–C electrocatalyst *via* space-confined control of nitrogen-doping efficiency and the molecular-level coordination effect,” *J. Mater. Chem. A*, vol. 6, no. 27, pp. 13050–13061, 2018, doi: 10.1039/C8TA03759K.
[51] V. Chipakwe, P. Semsari, T. Karlkvist, J. Rosenkranz, and S. C. Chelgani, “A critical review on the mechanisms of chemical additives used in grinding and their effects on the downstream processes,” *J. Mater. Res. Technol.*, vol. 9, no. 4, pp. 8148–8162, Jul. 2020, doi: 10.1016/j.jmrt.2020.05.080.
[52] P. Rao *et al.*, “Plasma induced Fe-N active sites to improve the oxygen reduction reaction performance,” *Adv. Sens. Energy Mater.*, vol. 1, no. 1, p. 100005, Mar. 2022, doi: 10.1016/j.asems.2022.100005.
[53] J. H. Kim, Y. J. Sa, H. Y. Jeong, and S. H. Joo, “Roles of Fe−N $_x$ and Fe−Fe $_3$ C@C Species in Fe−N/C Electrocatalysts for Oxygen Reduction Reaction,” *ACS Appl. Mater. Interfaces*, vol. 9, no. 11, pp. 9567–9575, Mar. 2017, doi: 10.1021/acsami.6b13417.
[54] S. Lee, L. Bai, and X. Hu, “Deciphering Iron-Dependent Activity in Oxygen Evolution Catalyzed by Nickel–Iron Layered Double Hydroxide,” *Angew. Chem. Int. Ed.*, vol. 59, no. 21, pp. 8072–8077, May 2020, doi: 10.1002/anie.201915803.
[55] L. Ma *et al.*, “Single-Site Active Iron-Based Bifunctional Oxygen Catalyst for a Compressible and Rechargeable Zinc–Air Battery,” *ACS Nano*, vol. 12, no. 2, pp. 1949–1958, Feb. 2018, doi: 10.1021/acsnano.7b09064.
[56] J. Zhang *et al.*, “A defect-driven atomically dispersed Fe–N–C electrocatalyst for bifunctional oxygen electrocatalytic activity in Zn–air batteries,” *J. Mater. Chem. A*, vol. 9, no. 9, pp. 5556–5565, 2021, doi: 10.1039/D0TA11859A.
[57] X. Zhao, L. Shao, Z. Wang, H. Chen, H. Yang, and L. Zeng, “*In situ* atomically dispersed Fe doped metal-organic framework on reduced graphene oxide as bifunctional electrocatalyst for Zn–air batteries,” *J. Mater. Chem. C*, vol. 9, no. 34, pp. 11252–11260, 2021, doi: 10.1039/D1TC02729H.
[58] E. Hu, X.-Y. Yu, F. Chen, Y. Wu, Y. Hu, and X. W. D. Lou, “Graphene Layers-Wrapped Fe/Fe $_5$ C $_2$ Nanoparticles Supported on N-doped Graphene Nanosheets for Highly Efficient Oxygen Reduction,” *Adv. Energy Mater.*, vol. 8, no. 9, p. 1702476, Mar. 2018, doi: 10.1002/aenm.201702476.
[59] L. Osmieri, R. Escudero-Cid, A. H. A. Monteverde Videla, P. Ocón, and S. Specchia, “Performance of a Fe-N-C catalyst for the oxygen reduction reaction in direct methanol fuel cell: Cathode formulation optimization and short-term durability,” *Appl. Catal. B Environ.*, vol. 201, pp. 253–265, Feb. 2017, doi: 10.1016/j.apcatb.2016.08.043.
[60] N. Bhuvanendran, S. Ravichandran, K. Peng, S. S. Jayaseelan, Q. Xu, and H. Su, “Highly durable carbon supported FE□N nanocrystals feature as efficient bi-functional oxygen electrocatalyst,” *Int. J. Energy Res.*, vol. 44, no. 11, pp. 8413–8426, Sep. 2020, doi: 10.1002/er.5524.

[61] S. Trasatti and O. A. Petrii, “Real surface area measurements in electrochemistry,” *Pure Appl. Chem.*, vol. 63, no. 5, pp. 711–734, Jan. 1991, doi: 10.1351/pac199163050711.
[62] C. C. L. McCrory, S. Jung, J. C. Peters, and T. F. Jaramillo, “Benchmarking Heterogeneous Electrocatalysts for the Oxygen Evolution Reaction,” *J. Am. Chem. Soc.*, vol. 135, no. 45, pp. 16977–16987, Nov. 2013, doi: 10.1021/ja407115p.
[63] Y. Li and C. Zhao, “Enhancing Water Oxidation Catalysis on a Synergistic Phosphorylated NiFe Hydroxide by Adjusting Catalyst Wettability,” *ACS Catal.*, vol. 7, no. 4, pp. 2535–2541, Apr. 2017, doi: 10.1021/acscatal.6b03497.
[64] P. Connor, J. Schuch, B. Kaiser, and W. Jaegermann, “The Determination of Electrochemical Active Surface Area and Specific Capacity Revisited for the System $MnO_x$ as an Oxygen Evolution Catalyst,” *Z. Für Phys. Chem.*, vol. 234, no. 5, pp. 979–994, May 2020, doi: 10.1515/zpch-2019-1514.
[65] W.-J. Jiang *et al.*, “Understanding the High Activity of Fe–N–C Electrocatalysts in Oxygen Reduction: $Fe/Fe_3C$ Nanoparticles Boost the Activity of $Fe–N_x$,” *J. Am. Chem. Soc.*, vol. 138, no. 10, pp. 3570–3578, Mar. 2016, doi: 10.1021/jacs.6b00757.
[66] J. Qi, W. Zhang, and R. Cao, “Porous Materials as Highly Efficient Electrocatalysts for the Oxygen Evolution Reaction,” *ChemCatChem*, vol. 10, no. 6, pp. 1206–1220, Mar. 2018, doi: 10.1002/cctc.201701637.
[67] J.-S. M. Lee, S. Sarawutanukul, M. Sawangphruk, and S. Horike, “Porous Fe–N–C Catalysts for Rechargeable Zinc–Air Batteries from an Iron-Imidazolate Coordination Polymer,” *ACS Sustain. Chem. Eng.*, vol. 7, no. 4, pp. 4030–4036, Feb. 2019, doi: 10.1021/acssuschemeng.8b05403.
[68] Y. Niu *et al.*, “Space-Confined Strategy to $Fe_7C_3$ Nanoparticles Wrapped in Porous Fe-/N-Doped Carbon Nanosheets for Efficient Oxygen Electrocatalysis,” *ACS Sustain. Chem. Eng.*, vol. 7, no. 15, pp. 13576–13583, Aug. 2019, doi: 10.1021/acssuschemeng.9b03794.
[69] J. Sheng, S. Zhu, G. Jia, X. Liu, and Y. Li, “Carbon nanotube supported bifunctional electrocatalysts containing iron-nitrogen-carbon active sites for zinc-air batteries,” *Nano Res.*, vol. 14, no. 12, pp. 4541–4547, Dec. 2021, doi: 10.1007/s12274-021-3369-0.
[70] K. Miyazaki, Y. S. Lee, T. Fukutsuka, and T. Abe, “Suppression of Dendrite Formation of Zinc Electrodes by the Modification of Anion-Exchange Ionomer,” *Electrochemistry*, vol. 80, no. 10, pp. 725–727, 2012, doi: 10.5796/electrochemistry.80.725.
[71] J. Fu, Z. P. Cano, M. G. Park, A. Yu, M. Fowler, and Z. Chen, “Electrically Rechargeable Zinc-Air Batteries: Progress, Challenges, and Perspectives,” *Adv. Mater.*, vol. 29, no. 7, p. 1604685, Feb. 2017, doi: 10.1002/adma.201604685.
[72] L. Guo, H. Guo, H. Huang, S. Tao, and Y. Cheng, “Inhibition of Zinc Dendrites in Zinc-Based Flow Batteries,” *Front. Chem.*, vol. 8, p. 557, Jul. 2020, doi: 10.3389/fchem.2020.00557.

## Non-exclusive licence to reproduce the thesis and make the thesis public

I, Amina Alimbekova,

1. grant the University of Tartu a free permit (non-exclusive licence) to:

reproduce, for the purpose of preservation, including for adding to the DSpace digital archives until the expiry of the term of copyright, my thesis

"Mechanochemical Production of Non-Precious Bifunctional Fe-N-C Electrocatalysts",

supervised by Akmal Kosimov and Nadežda Kongi,

2. I grant the University of Tartu the permit to make the thesis specified in point 1 available to the public via the web environment of the University of Tartu, including via the DSpace digital archives, under the Creative Commons licence CC BY NC ND 4.0, which allows, by giving appropriate credit to the author, to reproduce, distribute the work and communicate it to the public, and prohibits the creation of derivative works and any commercial use of the work from ***27/05/2024*** until the expiry of the term of copyright,
3. I am aware that the author retains the rights specified in points 1 and 2.

4. I confirm that granting the non-exclusive licence does not infringe other persons' intellectual property rights or rights arising from the personal data protection legislation.

*Amina Alimbekova*

***27/05/2022***